SENSORCOMM 2021

The Fifteenth International Conference on Sensor Technologies and Applications

ISBN: 978-1-61208-917-1

November 14 - 18, 2021

Athens, Greece

SENSORCOMM 2021 Editors

Anne-Lena Kampen, Western Norway University of Applied Sciences, Norway
Oana Dini, IARIA, EU/USA
Hesham Ali, University of Nebraska at Omaha, USA
Laura Garcia, Universitat Politècnica de València (UPV), Spain

SENSORCOMM 2021

Forward

The Fifteenth International Conference on Sensor Technologies and Applications (SENSORCOMM 2021), held on November 14-18, 2021, was a multi-track event covering related topics on theory and practice on wired and wireless sensors and sensor networks.

Sensors and sensor networks have become a highly active research area because of their potential of providing diverse services to broad range of applications, not only on science and engineering, but equally importantly on issues related to critical infrastructure protection and security, health care, the environment, energy, food safety, and the potential impact on the quality of all areas of life.

Sensor networks and sensor-based systems support many applications today on the ground. Underwater operations and applications are quite limited by comparison. Most applications refer to remotely controlled submersibles and wide-area data collection systems at a coarse granularity.

In wireless sensor and micro-sensor networks energy consumption is a key factor for the sensor lifetime and accuracy of information. Protocols and mechanisms have been proposed for energy optimization considering various communication factors and types of applications. Conserving energy and optimizing energy consumption are challenges in wireless sensor networks, requiring energy-adaptive protocols, self-organization, and balanced forwarding mechanisms.

We take here the opportunity to warmly thank all the members of the SENSORCOMM 2021 technical program committee, as well as all the reviewers. The creation of such a high quality conference program would not have been possible without their involvement. We also kindly thank all the authors who dedicated much of their time and effort to contribute to SENSORCOMM 2021. We truly believe that, thanks to all these efforts, the final conference program consisted of top quality contributions.

We also thank the members of the SENSORCOMM 2021 organizing committee for their help in handling the logistics and for their work that made this professional meeting a success.

We hope that SENSORCOMM 2021 was a successful international forum for the exchange of ideas and results between academia and industry and to promote further progress in the area of sensor technologies and applications.

SENSORCOMM 2021 Chairs

SENSORCOMM 2021 Steering Committee
Anne-Lena Kampen, Western Norway University of Applied Sciences, Norge
Masanari Nakamura, Hokkaido University, Japan

SENSORCOMM 2021 Publicity Chair
Mar Parra Boronat, Universitat Politecnica de Valencia, Spain
Sandra Viciano Tudela, Universitat Politecnica de Valencia, Spain

SENSORCOMM 2021

Committee

SENSORCOMM 2021 Steering Committee
Anne-Lena Kampen, Western Norway University of Applied Sciences, Norge
Masanari Nakamura, Hokkaido University, Japan

SENSORCOMM 2021 Publicity Chair
Mar Parra Boronat, Universitat Politecnica de Valencia, Spain
Sandra Viciano Tudela, Universitat Politecnica de Valencia, Spain

SENSORCOMM 2021 Technical Program Committee

Majid Bayani Abbasy, National University of Costa Rica, Costa Rica
Amin Al-Habaibeh, Nottingham Trent University, UK
Haitham Al-Obiedollah, The Hashemite University, Jordan
Jesús B. Alonso Hernández, Institute for Technological Development and Innovation in Communications (IDeTIC) | University of Las Palmas de Gran Canaria (ULPGC), Spain
Youssef N. Altherwy, Imperial College London, UK
Mário Alves, Politécnico do Porto - School of Engineering (ISEP), Portugal
Thierry Antoine-Santoni, University of Corsica, France
Kazutami Arimoto, Okayama Prefectural University, Japan
Anish Arora, The Ohio State University / The Samraksh Company, USA
Andy Augousti, Kingston University London, UK
Michel Bakni, ESTIA Recherche, Bidart, France
Reda Benkhouya, Ibn Tofail University, Morocco
Souheila Bouam, University of Batna 2, Algeria
An Braeken, Vrije Universiteit België, Belgium
Erik Buchmann, Hochschule für Telekommunikation Leipzig, Germany
Juan-Vicente Capella-Hernández, Universitat Politècnica de València, Spain
Oscar Carrasco Quilis, Casa Systems Inc., Valencia, Spain
Vítor Carvalho**,** 2Ai Lab- School of Technology - IPCA / Algoritmi Research Center - Minho University, Portugal
Mario Cifrek, University of Zagreb, Croatia
Federico Corò, Sapienza University of Rome, Italy
Luis J. de la Cruz Llopis, Universitat Politècnica de Catalunya, Spain
Baban P. Dhonge, Indira Gandhi Center for Atomic Research, Kalpakkam, India
Alexis Duque, Rtone, Lyon, France
Loubna El Amrani, Ibn University Tofail Kénitra, Morocco
Mohamed El Bakkali, Sidi Mohamed Ben Abdellah University, Morocco
Youssef Elgholb, University Sidi Mohamed Ben Abdellah, Fez, Morocco / Technical University of Cartagena, Spain
Biyi Fang, Microsoft Corporation, USA
Stefan Fischer, University of Lübeck, Germany
Beatriz Gallego-Nicasio Crespo, Atos Research & Innovation, Spain

Copyright Information

For your reference, this is the text governing the copyright release for material published by IARIA.

The copyright release is a transfer of publication rights, which allows IARIA and its partners to drive the dissemination of the published material. This allows IARIA to give articles increased visibility via distribution, inclusion in libraries, and arrangements for submission to indexes.

I, the undersigned, declare that the article is original, and that I represent the authors of this article in the copyright release matters. If this work has been done as work-for-hire, I have obtained all necessary clearances to execute a copyright release. I hereby irrevocably transfer exclusive copyright for this material to IARIA. I give IARIA permission or reproduce the work in any media format such as, but not limited to, print, digital, or electronic. I give IARIA permission to distribute the materials without restriction to any institutions or individuals. I give IARIA permission to submit the work for inclusion in article repositories as IARIA sees fit.

I, the undersigned, declare that to the best of my knowledge, the article is does not contain libelous or otherwise unlawful contents or invading the right of privacy or infringing on a proprietary right.

Following the copyright release, any circulated version of the article must bear the copyright notice and any header and footer information that IARIA applies to the published article.

IARIA grants royalty-free permission to the authors to disseminate the work, under the above provisions, for any academic, commercial, or industrial use. IARIA grants royalty-free permission to any individuals or institutions to make the article available electronically, online, or in print.

IARIA acknowledges that rights to any algorithm, process, procedure, apparatus, or articles of manufacture remain with the authors and their employers.

I, the undersigned, understand that IARIA will not be liable, in contract, tort (including, without limitation, negligence), pre-contract or other representations (other than fraudulent misrepresentations) or otherwise in connection with the publication of my work.

Exception to the above is made for work-for-hire performed while employed by the government. In that case, copyright to the material remains with the said government. The rightful owners (authors and government entity) grant unlimited and unrestricted permission to IARIA, IARIA's contractors, and IARIA's partners to further distribute the work.

Table of Contents

LiDAR-Based Cooperative Scan Matching for Relative Pose Estimation of Multiple Vehicles in GNSS-Denied Environments

Ryoga Takahashi
Graduate School of Science and Engineering
Doshisha University
Kyotanabe, Kyoto 610-0394 Japan

Masafumi Hashimoto, Kazuhiko Takahashi
Faculty of Science and Engineering
Doshisha University
Kyotanabe, Kyoto 610-0394 Japan
e-mail: {mhashimo, katakaha}@mail.doshisha.ac.jp

***Abstract*—This paper presents a relative pose estimation method for multiple vehicles that involves scan matching using Light Detection And Ranging (LiDAR) measurements captured from overlapping sensing areas of neighboring vehicles. Such Cooperative Scan Matching (CSM) can be used to Cooperative Moving-Object Tracking (CMOT) by vehicles in Global Navigation Satellite Systems (GNSS)-denied environments. Each vehicle is equipped with a LiDAR and detects static measurements originating from static objects, such as building walls and utility poles, from its own LiDAR scan images by applying an occupancy grid method. Each vehicle then obtains point feature histograms related to static features using Fast Point Feature Histograms (FPFH). The information related to LiDAR measurements and point feature histograms is sent to a central server. After the central server matches the environmental features obtained by the vehicles based on point feature histograms and estimates the relative pose of the vehicles by RAaNdom Sample Consensus (RANSAC) based coarse registration and Normal Distributions Transform (NDT) scan matching-based fine registration. Experimental results using two LiDAR-equipped vehicles in two road environments show that the proposed CSM has better applicability in urban environments with a high number of streets.**

Keywords-multi-vehicles; LiDAR; cooperative scan matching; relative pose estimation; FPFH; NDT scan mathcing.

I. INTRODUCTION

Tracking (i.e., estimating the position, size, and velocity) of multiple moving objects such as people, cars, bicycles, and motorcycles in real environments is an important issue for the safe navigation and autonomous driving of mobile robots and vehicles [1]–[3]. For such Moving-Object Tracking (MOT), the use of stereo camera, Light Detection And Ranging (LiDAR), and radar in mobile robotics and Intelligent Transportation Systems (ITS) has been drawing considerable interest. This paper focuses on LiDAR-based MOT.

MOT using only a LiDAR mounted on a vehicle (called Individual MOT (IMOT)) cannot track moving objects that exist outside the sensing area of the vehicle or in a blind spot of the vehicle. To address this problem of IMOT, Cooperative Moving-Object Tracking (CMOT) [4] and cooperative perception (CP) [5][6] have been presented. Multiple vehicles exchange LiDAR sensing data through a vehicle-to-vehicle communication network, and they detect and track moving objects in each other's blind spots. CMOT and CP can then improve the accuracy and reliability of MOT and environmental sensing.

In MOT, the occupancy grid method [7] is usually used to detect moving objects from the LiDAR measurements. In this method, the accurate self-pose (position and attitude) of the LiDAR-equipped vehicle in the world coordinate frame is required to map the LiDAR measurements acquired in the sensor coordinate frame onto the grid map in the world coordinate frame. In CMOT, if the accuracy of self-pose estimation in the world coordinate frame differs from vehicle to vehicle, each vehicle would misrecognize the same object as two different objects. In addition, it would recognize an object's size as larger or smaller than the actual size.

For accurate self-pose estimation of vehicles in CMOT, we used Real Time Kinematic Global Navigation Satellite Systems (RTK GNSS) under the assumption that CMOT is applied in outdoor open-sky environments [8]. However, GNSS, including RTK GNSS, lack credibility due to the multipath or mask effects in urban street canyons. CMOT can be performed in such GNSS-denied environments using Cooperative Scan Matching (CSM) [9] and cooperative positioning [10][11]. CSM estimates the relative pose of vehicles by matching the LiDAR measurements in the overlapping sensing areas of these vehicles, and the self-poses of the vehicles are corrected using the relative pose estimate. Iterative Closest Point (ICP) [12] or Normal Distributions Transforms (NDT) -based scan matching [13] are used as CSM algorithms.

In relative pose estimation using ICP or NDT-based scan matching (called fine registration), an appropriate initial value of the relative pose (called coarse registration) should be calculated to avoid the local-minimum problem in the iterative calculation in the fine registration. Our previous work [9] extracted pole-like objects in environments, such as utility poles and light poles, from the LiDAR measurements and utilized them as environmental features for coarse registration. However, many environments do not have such objects. In addition, where they do exist, they are frequently occluded by surrounding moving objects, such as cars, tracks, and buses.

This paper presents a coarse registration method that uses Fast Point Feature Histograms (FPFH) and Random Sample Consensus (RANSAC)-based algorithm [14][15]. Since such coarse registration does not limit the environmental features to pole-like objects, it can be applied in various GNSS-

 ISBN: 978-1-61208-917-1

denied environments, such as urban city roads and roads with many street trees. In this paper, NDT scan matching-based fine registration is used to estimate the relative pose of vehicles. In addition, a success/failure decision method of CSM is presented.

The rest of this paper is organized as follows: Section II provides an overview of our experimental system and CMOT method. Section III describes the relative pose estimation by CSM and the success/failure decision. In Section IV, experimental results obtained in outdoor road environments by two vehicles (small electric car and motorcycle) are shown, followed by our conclusions in Section V.

II. EXPERIMENTAL SYSTEM AND CMOT OVERVIEW

In this section, an overview of our experimental system and CMOT is presented.

A. Experimental System

Figure 1 shows the two experimental vehicles: a small electric car (Toyota auto body, COMS) and a motorcycle (Honda, Gyro Canopy). A 32-layer scanning LiDAR (Velodyne, HDL-32E) is installed on the top of each vehicle. The maximum range of the LiDAR is 70 m, the horizontal viewing angle is 360° with a resolution of 0.16°, and the vertical viewing angle is 41.34° with a resolution of 1.33°. The LiDAR provides 384 measurements (the object's 3D position and reflection intensity) every 0.55 ms (at 2° horizontal angle increments). The period needed for the laser beam to complete one rotation (360°) in the horizontal direction is 100 ms; thus 70,000 measurements are obtained in one rotation.

The motorcycle (vehicle 2) is also equipped with Inertial Measurement Unit (IMU) (Xsens, MTi-300). The IMU outputs the attitude angle (roll and pitch angles) and angular velocity (roll, pitch, and yaw angular velocities) every 10 ms. The errors in attitude angle and angular velocity are less than ±0.3° and ±0.2°/s, respectively.

B. Overview of CMOT

Figure 2 shows a sequence of CMOT. Each vehicle senses its surrounding environment with its scanning LiDAR. The LiDAR obtains range measurements by scanning laser beams. Thus, when the vehicle moves, the entire scan data within one scan (laser beam rotation of 360° in the horizontal plane) cannot be obtained at the same pose of the vehicle. Therefore, if the entire scan data obtained within one scan are mapped onto the world coordinate frame using the self-pose information of the vehicle, distortion will arise in the LiDAR scan images. To correct this distortion, the vehicle's pose is determined in a period shorter than than the LiDAR scan period, i.e., for every LiDAR measurement (0.55 ms) in the scan. Vehicle 1 (small car) corrects the distortion in the LiDAR scan images using the information from only LiDAR measurements [16]. Vehicle 2 (motorcycle) corrects the distortion using the information from its LiDAR and IMU measurements because it changes its pose more significantly compared with vehicle 1 [17].

(a) Vehicle 1 (small car)

(b) Vehicle 2 (scooter)

Figure 1. Overview of the experimental vehicle.

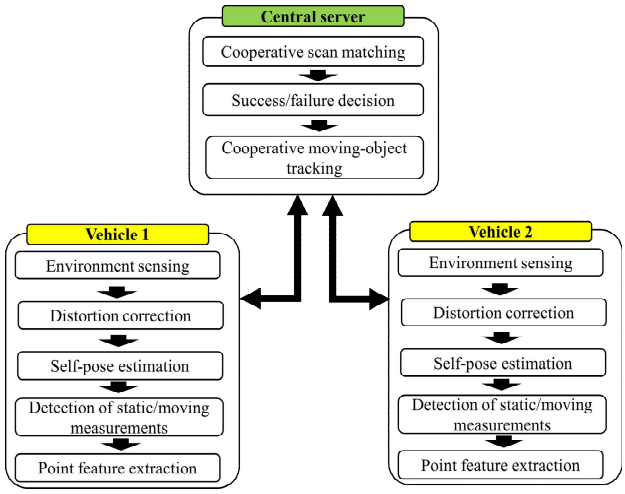

Figure 2. Overview of the cooperative moving-object tracking (CMOT).

Each vehicle maps their corrected LiDAR measurements onto the grid map. Based on the occupancy grid method, the LiDAR measurements are classified into two types, namely moving and static measurements, which originate from moving and static objects, respectively. Point feature histograms are obtained using FPFH for static measurements.

 ISBN: 978-1-61208-917-1

The information of the LiDAR measurements is then uploaded to the central server. This information includes time stamps, 3D positions of static measurements with the point feature histograms, 3D positions of the moving measurements, and self-poses of the vehicles.

After receiving the information of the LiDAR measurements, the central server estimates the size, position, and velocity of the moving objects using a Bayesian-based algorithm [10]. The estimated information is then fed back to the vehicles.

In this paper, NDT-based Simultaneous Localization and Mapping (SLAM) [19] is assumed to estimate the self-poses of the vehicles. In CMOT, if two vehicles have different accuracies of their self-poses in the world coordinate frame, the mapping of LiDAR measurements for the same object onto the grid map will cause errors, and the CMOT performance will deteriorate. Therefore, the relative pose between two vehicles is estimated by CSM, and the self-poses of the vehicles are corrected using the relative pose information. In this paper, for simplicity, only the self-pose of vehicle 2 is corrected.

CSM estimates the relative pose between two vehicles by matching the static measurements in the overlapping sensing areas of the vehicles using NDT scan matching. However, if the initial pose given to NDT scan matching is inaccurate, NDT scan matching will output an inaccurate relative pose due to the local-minimum problem in its iterative calculation. Therefore, the static measurements in the overlapping sensing areas of two vehicles are matched based on the point feature histograms, and the relative pose is coarsely estimated using RANSAC. The relative pose estimate obtained by such coarse registration is given to NDT scan matching as the initial pose.

Finally, the success or failure of CSM is assessed. If it is deemed successful, the moving measurements detected by two vehicles are re-mapped to the grid map, and the moving objects are tracked.

III. COOPERATIVE SCAN MATCHING

In this section, the point feature histograms obtained using FPFH, which is a metric for matching static measurements from two LiDARs, are first described. Next, the relative pose between two vehicles is estimated using coarse and fine registration. Finally, the success/failure decision method of CSM is described.

A. Point Feature Histograms

Each vehicle obtains point features using FPFH [14] from the static measurements. Vehicle 1 first maps the static measurements onto a voxel map (grid size of 1 m) in its own vehicle coordinate frame Σ_1 (fixed to vehicle 1) and downsamples the static measurements using a voxel grid filter. The centroid of the static measurements in the i-th voxel (i = 1, 2, …) on the voxel map is then obtained. The centroid is called the feature point A_i. Vehicle 2 obtains the feature point B_i in the same way from the static measurements in its own coordinate frame Σ_2.

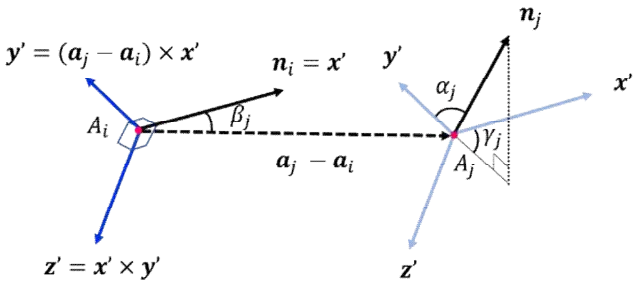

Figure 3. Point feature.

The point feature histograms are calculated based on the feature points A_i and B_i. Since it is the same for both vehicles, only the point feature histograms calculation method for vehicle 1 is described in this paper.

The 3D position of the feature point A_i in the i-th voxel is denoted by $\boldsymbol{a}_i$ in Σ_1. The 3D position of the feature point A_j in the j-voxel (j =1, 2, ... 124), which is located around the i-th voxel, is also denoted by $\boldsymbol{a}_j$ in Σ_1. As shown in Figure 3, the normal vectors for the feature points A_i and A_j are denoted by $\boldsymbol{n}_i$ and $\boldsymbol{n}_j$, respectively. A coordinate frame Σ_{Ai} is defined, in which the feature point A_i is used as the origin O_{Ai}, the normal vector $\boldsymbol{n}_i$ as the x' axis, $(\boldsymbol{a}_j - \boldsymbol{a}_i) \times \boldsymbol{x}'$ as the y' axis, and the axis orthogonal to the x' and y' axes as the z' axis.

Then, the triple feature (α_j, β_j, γ_j) related to the angles in Σ_{Ai} is defined by $\alpha_j = \boldsymbol{y}' \cdot \boldsymbol{n}_j$, $\beta_j = \boldsymbol{x}' \cdot (\boldsymbol{a}_j - \boldsymbol{a}_i)$, and $\gamma_j = \arctan(\boldsymbol{z}' \cdot \boldsymbol{n}_j / \boldsymbol{x}' \cdot \boldsymbol{n}_j)$. The point features $\boldsymbol{SPFH}(A_i)$ of 3×124-dimensional vector is obtained by calculating the features for the 124 feature points A_j (j =1, 2, ... 124) around A_i. In similar way, the point features $\boldsymbol{SPFH}(A_j)$ for the feature points A_j (j =1, 2, ... 124) around A_i are obtained. The final histograms (33 dimensions) related to the feature point A_i are then determined from

$$\boldsymbol{FPFH}(A_i) = \boldsymbol{SPFH}(A_i) + \frac{1}{124} \sum_{j=1}^{124} \frac{1}{w_j} \boldsymbol{SPFH}(A_j) \quad (1)$$

where the weight w_j is equal to $\left| \boldsymbol{a}_j - \boldsymbol{a}_i \right|$.

B. Relative Pose Estimation

In the coarse registration, the relative pose between vehicles is determined by matching the feature points A_i and B_i with similar point feature histograms. However, since many feature points have similar feature histograms, incorrect matching often occurs. Therefore, the following RANSAC-based method is used to perform the coarse registration.

Step 1: Three feature points A_i^* (i = 1, 2, 3) are randomly extracted from the set of feature points obtained by vehicle 1. Then, 100 feature points B_i (i = 1, … 100) with similar feature histograms as those of A_i^* are extracted using the k-nearest neighbor method from the set of feature points obtained by vehicle 2. Then, one feature point B_i^* is randomly selected from the 100 feature points B_i.

Step 2: The pose of vehicle 2 relative to vehicle 1 is denoted by $\delta \boldsymbol{X} = (\delta x, \delta y, \delta z, \delta\phi, \delta\theta, \delta\psi)^T$, where $\delta \boldsymbol{x}=(\delta x,\delta y,\delta z)^T$ and $\delta \boldsymbol{\theta}=(\delta\phi,\delta\theta,\delta\psi)^T$ are the relative position and attitude angle (roll, pitch, and yaw angles), respectively.

The centroid positions of three feature points (A_1^*, A_2^*, A_3^*) and (B_1^*, B_2^*, B_3^*) are denoted by $\bar{\boldsymbol{a}}$ and $\bar{\boldsymbol{b}}$, respectively. The feature point matrices are denoted by $\delta \boldsymbol{a}=(\delta \boldsymbol{a}_1, \delta \boldsymbol{a}_2, \delta \boldsymbol{a}_3)^T$ and $\delta \boldsymbol{b}=(\delta \boldsymbol{b}_1, \delta \boldsymbol{b}_2, \delta \boldsymbol{b}_3)^T$, where $\delta \boldsymbol{a}_i \triangleq \boldsymbol{a}_i^* - \bar{\boldsymbol{a}}$ and $\delta \boldsymbol{b}_i \triangleq \boldsymbol{b}_i^* - \bar{\boldsymbol{b}}$, and $\boldsymbol{a}_i^*$ and $\boldsymbol{b}_i^*$ are the 3D positions of the feature points A_i^* and B_i^*, respectively. With use of the matrices $\boldsymbol{U}$ and $\boldsymbol{V}$, which are defined by the singular value decomposition ($\boldsymbol{H} = \boldsymbol{U\Sigma V}^T$) of the matrix $\boldsymbol{H} = \delta \boldsymbol{b} \bullet \delta \boldsymbol{a}^T$, the relative position $\delta \boldsymbol{x}$ and the rotational matrix $\boldsymbol{R}(\delta\boldsymbol{\theta})$ related to the relative attitude angle $\delta\boldsymbol{\theta}$ are given by

$$\boldsymbol{R}(\delta\boldsymbol{\theta}) = \boldsymbol{V}\boldsymbol{U}^T = \begin{pmatrix} \cos\delta\theta\cos\delta\psi & \sin\delta\phi\sin\delta\theta\cos\delta\psi - \cos\delta\phi\sin\delta\psi & \cos\delta\phi\sin\delta\theta\cos\delta\psi + \sin\delta\phi\sin\delta\psi \\ \cos\delta\theta\sin\delta\psi & \sin\delta\phi\sin\delta\theta\sin\delta\psi + \cos\delta\phi\cos\delta\psi & \cos\delta\phi\sin\delta\theta\sin\delta\psi - \sin\delta\phi\cos\delta\psi \\ -\sin\delta\theta & \sin\delta\phi\cos\delta\theta & \cos\delta\phi\cos\delta\theta \end{pmatrix} \quad (2)$$

$$\delta \boldsymbol{x} = \bar{\boldsymbol{a}} - \boldsymbol{R}(\delta\boldsymbol{\theta})\bar{\boldsymbol{b}} \quad (3)$$

With use of the relative pose, the 3D position $\boldsymbol{b}_i$ of the feature point B_i in Σ_2 (obtained by vehicle 2) can be transformed to the 3D position $\boldsymbol{b}_i^{(1)}$ in Σ_1. The feature point nearest to $\boldsymbol{b}_i^{(1)}$ is extracted from the set of feature points A_i (i =1, 2, ...), and the 3D position of the nearest feature point in Σ_1 is denoted by $\tilde{\boldsymbol{a}}_i$. Then, the cost function is given by

$$J = \frac{1}{N_B}\sum_{i=1}^{N_B} (\tilde{\boldsymbol{a}}_i - \boldsymbol{b}_i^{(1)})^T (\tilde{\boldsymbol{a}}_i - \boldsymbol{b}_i^{(1)}) \quad (4)$$

where $\boldsymbol{b}_i^{(1)} = \boldsymbol{R}(\delta\boldsymbol{\theta})\boldsymbol{b}_i + \delta \boldsymbol{x}$. N_B is the number of the feature points B_i.

Step 3: Steps 1 and 2 are repeated 10,000 times to find the relative pose $\delta\boldsymbol{X}$ with the smallest J. Then, the relative pose $\delta\boldsymbol{X}_0$ is obtained in the coarse registration.

In NDT scan matching, the relative pose $\delta\boldsymbol{X}_0$ is used as the initial value, and the iterative calculation is performed using the Newton method to maximize the likelihood function in Eq. (5). The relative pose $\delta\boldsymbol{X}^*$ can then be obtained.

$$\Lambda = \prod_{j=1}^{N_2} \exp\left(-\frac{1}{2} (\boldsymbol{q}_j^{(1)} - \bar{\boldsymbol{p}}_i)^T \boldsymbol{\Omega}_i^{-1} (\boldsymbol{q}_j^{(1)} - \bar{\boldsymbol{p}}_i) \right) \quad (5)$$

where $\bar{\boldsymbol{p}}_i$ and $\boldsymbol{\Omega}_i$ are the mean and covariance, respectively, of the 3D positions of the static measurements in the i-th voxel of the voxel map in Σ_1. $\boldsymbol{q}_j$ is the 3D position of the j-th static measurement (j = 1, 2, $\cdots N_2$) obtained by vehicle 2 in Σ_2 and transformed to Σ_1.

C. Success/Failure Decision

Determination of CSM success or failure is vital (i.e. whether the relative pose obtained by CSM is correct or not).

After the NDT scan matching-based fine registration, the static measurements are first downsampled with a voxel grid filter (cell size of 0.5 m in this paper). The sets of downsampled static measurements related to vehicles 1 and 2 are called static measurement sets 1 and 2, respectively. For each measurement in static measurement sets 2, the closest measurement is identified from static measurement sets 1, and the Euclidean distance between the two measurements is calculated. This process is conducted M_2 times, where M_2 is the number of measurements in static measurement sets 2. The number M_{near} of static measurements whose Euclidean distance is 0.5 m or less is counted.

The matching rate is defined by $M_{near} \diagup M_2$. If the matching rate is equal to or greater than a threshold (33% in this paper), then the CSM is deemed successful, and the relative pose obtained by the CSM is utilized in CMOT.

The computational cost related to the coarse registration is high. Therefore, if the CSM is found to succeed in the current scan, the coarse registration will not be executed in the next scan. The relative pose estimated by the NDT scan matching in the current scan is then used as the initial pose for the NDT scan matching in the next scan. By contrast, if the CSM is found to have failed in the current scan, both the coarse and fine registration is utilized to estimate the relative pose in the next scan.

IV. Experimental Results

Experiments are conducted in two environments: an urban road environment with many buildings (environment 1; Figure 4 (a)) and a road environment with street trees (environment 2; Figure 5 (a)). In environment 1, vehicle 1 follows vehicle 2, which moves at about 40 km/h. The distance between the two vehicles is shown in Figure 4 (b). On the road, there are 20 cars and 5 pedestrians. In environment 2, vehicle 1 follows vehicle 2, which moves at about 30 km/h, and the distance between the two vehicles is shown in Figure 5 (b). On the road, there are 3 cars and 10 pedestrians.

Figure 6 shows the mapping results of the LiDAR measurements captured by the two vehicles at 40 s in environment 1. The mapping performance is compared in the following cases.

Case 1: Mapping using relative pose estimate by CSM (proposed method)
Case 2: Mapping using self-pose by RTK GNSS
Case 3: Mapping using self-pose by standard GNSS

The two experimental vehicles are equipped with RTK GNSS (Novatel ProPak-V3 on vehicle 1 and Novatel PwrPak7-E1 on vehicle 2) to evaluate our studies. In case 2, the LiDAR measurements captured by the two vehicles are mapped onto the world coordinate frame using the self-poses of the vehicles obtained by RTK GNSS. The GNSS in the normal mode (standard GNSS) is widely used in real-world

applications. However, the positioning accuracy of standard GNSS is worse than that of RTK GNSS. Thus, Gaussian errors with a mean of zero and standard deviation of 1 m are added to the self-pose obtained by RTK GNSS to generate the position information of standard GNSS. In case 3, LiDAR measurements are mapped onto the world coordinate frame using such pseudo-self-poses of the vehicles.

As shown in Figure 6 (d), in case 3, since the relative pose of the two vehicles is inaccurate, the LiDAR measurements related to the building walls and vehicles are not matched significantly. Then, the two detected vehicles will be recognized as four vehicles by our CMOT. In case 2 (Figure 6 (c)), although RTK GNSS gives an accurate relative pose between the two vehicles, the LiDAR measurements related to the building walls and vehicles are slightly mismatched. As shown in Figure 6 (b), the mapping performance of the proposed method (case 1) is better than that of the two other cases.

Figure 7 shows the mapping results of the LiDAR measurements captured by vehicles 1 and 2 at 14 s in environment 2. It is clear from this figure that the mapping performance of the proposed method (case 1) is better than that of the two other cases.

Table 1 shows the success rate of CSM and performance of CSM success/failure decision by the matching rate. Four measures are used to evaluate the performance of CSM success/failure decision: accuracy, precision, recall, and F-measure. The accuracy represents the ratio of the number of scans where the success/failure decision by the matching rate matches the actual success/failure result of CSM. Precision is the ratio of the number of scans where the CSM actually succeeds to the number of scans where the CSM is considered successful in the success/failure decision. Recall is the ratio of the number of scans where the CSM is found successful in the success/failure decision to the number of scans where the CSM actually succeeds. F-measure is the harmonic mean of precision and recall.

The success rate of CSM in environment 2 is lower than that in environment 1. As shown in Figures 4 (b) and 5 (b), the distance between the two vehicles in environment 2 is longer than that in environment 1. As the distance between the two vehicles increases, the overlapping area of the LiDARs decreases, and the inaccuracy of feature point matching increases. In addition, since the road environment with street trees (environment 2) has many similar point feature histograms, accurate feature point matching is difficult. Consequently, the success rate of CSM in environment 2 is lower than that in environment 1.

(a) Photo of environment (b) Distance between vehicles

Figure 4. Photo of environment and distance between vehicles (environment 1). The left photo is the bird's-eye view, and the yellow line in the left photo indicates the movement path of the vehicles.

(a) Photo of environment (b) Distance between vehicles

Figure 5. Photo of environment and distance between vehicles (environment 2). The left photo is the bird's-eye view, and the yellow line in the left photo indicates the movement path of the vehicles.

(a) Photo of environment

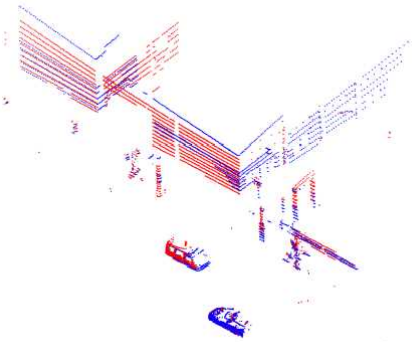

(b) Case 1 (using CSM)

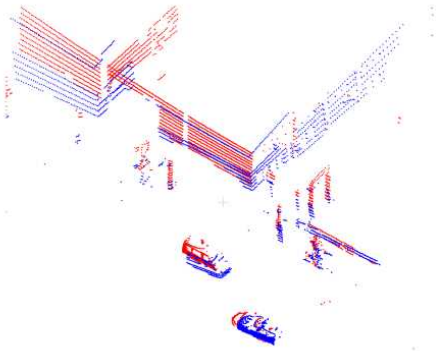

(c) Case 2 (using RTK GNSS)

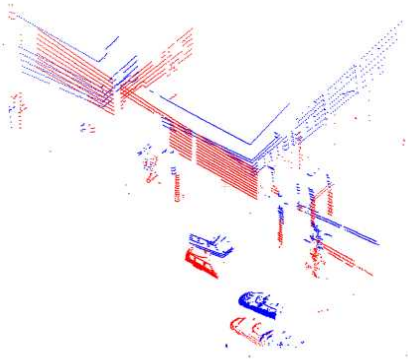

(d) Case 3 (using standard GNSS)

Figure 6. Mapping result in environment 1. The blue and red dots indicate the LiDAR measurements related to vehicles 1 and 2, respectively.

(a) Photo of environment

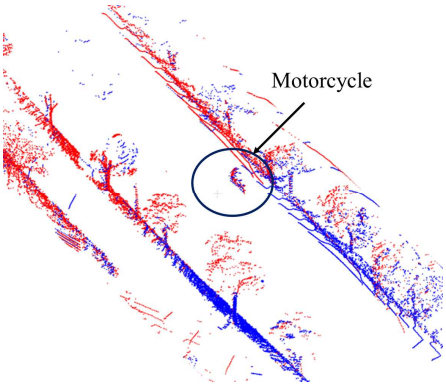

(b) Case 1 (using CSM)

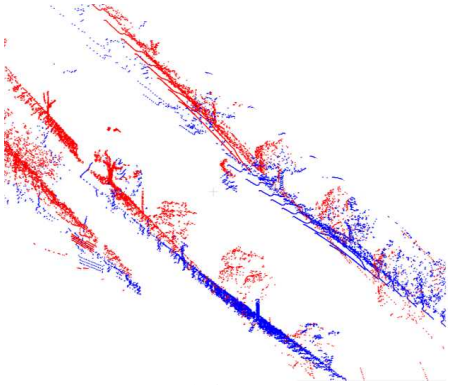

(c) Case 2 (using RTK GNSS)

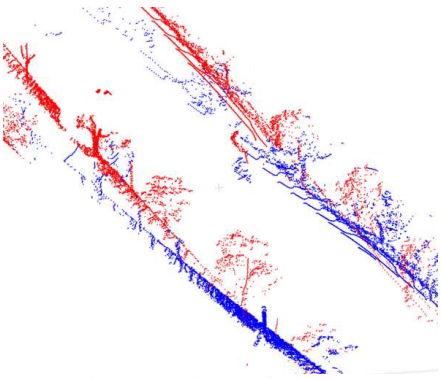

(d) Case 3 (using standard GNSS)

Figure 7. Mapping result in environment 2. The blue and red dots indicate the LiDAR measurements related to vehicles 1 and 2, respectively.

 ISBN: 978-1-61208-917-1

TABLE I. SUCCESS RATE OF CSM AND PERFORMANCE OF SUCCESS/FAILURE DECISION

		Environment 1	Environment 2
Success rate of CSM [%]		78.9	64.3
Performance of success/ failure decision	**Accuracy [%]**	95.5	87.4
	Precision [%]	97.8	86.1
	Recall [%]	96.6	99.0
	F-measure [%]	97.2	92.1

Table 1 also indicates that the performance of the CSM success/failure decision by the matching rate in environment 2 is considerably worse than that in environment 1. Since the road environment with street trees (environment 2) has many similar point feature histograms, incorrect matching frequently occurs. In consequence, the performance of the CSM success/failure decision is highly degraded in environment 2.

V. CONCLUSION AND FUTURE WORK

CMOT requires mapping LiDAR measurements captured by nearby vehicles onto a grid map represented on a common coordinate frame (e.g., world coordinate frame).

To accurately map these LiDAR measurements onto a grid map in GNSS-denied environments, this paper presented a relative pose estimation method that used CSM. Here, the relative pose between vehicles was estimated using the LiDAR measurements in the overlapping sensing areas of the vehicles. The relative pose estimation was performed using FPFH and RANSAC-based coarse registration and NDT scan matching-based fine registration. Experimental results using two LiDAR-equipped vehicles in two road environments showed that the proposed CSM has better applicability in urban environments with a high number of streets.

Since the spatial resolution of LiDAR is low in the vertical direction, the distance between vehicles where CSM can be achieved is short. Our current research effort aims to improve the CSM algorithm so that the relative pose can be estimated accurately even at long inter-vehicle distances. In addition, CSM will be implemented to CMOT and cooperative positioning.

REFERENCES

[1] E. Marti, J. Perez, M. A. Miguel, and F. Garcia, "A Review of Sensor Technologies for Perception in Automated Driving," IEEE Intelligent Transportation Systems Magazine, pp. 94–108, 2019.

[2] F. P. Muller, "Survey on Ranging Sensors and Cooperative Techniques for Relative Positioning of Vehicles," Sensors, vol. 17, 2017.

[3] E. Arnold, et al., "A Survey on 3D Object Detection Methods for Autonomous Driving Applications," IEEE Trans. on Intelligent Transportation Systems, vol.20, no.10, pp. 3782–3795, 2019.

[4] Y. Tamura, R. Murabayashi, M. Hashimoto, and K. Takahashi, "Hierarchical Cooperative Tracking of Vehicles and People Using Laser Scanners Mounted on Multiple Mobile Robots," Int. J. Advances in Intelligent Systems, vol. 10, pp. 90–101, 2017.

[5] Q. Chen, S. Tang, Q. Yangy, and S. Fuy, "Cooper: Cooperative Perception for Connected Autonomous Vehicles based on 3D Point Clouds," Proc. of IEEE 39th Int. Conf. on Distributed Computing Systems (ICDCS), 2019.

[6] M. Shan, et al., "Demonstrations of Cooperative Perception: Safety and Robustness in Connected and Automated Vehicle Operations," Sensors, 2021.

[7] A. Milstein, "Occupancy grid maps for localization and mapping. Motion Planning," Xing-Jian Jing, ed., InTech, pp. 382–408, 2008

[8] M. Ozaki, K. Kakinuma, M. Hashimoto, and K. Takahashi, "Laser Based Pedestrian Tracking in Outdoor Environments by Multiple Mobile Robots," Sensors, vol.12, pp.14489-14507, 2012.

[9] S. Kanaki, M. Hashimoto, Y. Yoden, and K. Takahashi, "Laser-based Cooperative Tracking of Vehicles and People by Multiple Mobile Robots in GNSS-denied Environments," Proc. of IEEE Int. Conf. on Advanced Intelligent Mechatronics (AIM), pp. 1228–1233, 2017.

[10] G. Soatti, et al., "Implicit Cooperative Positioning in Vehicular Networks," IEEE Trans. on Intelligent Transportation Systems, vol.19, issue 12, pp. 3964 –3980, 2018.

[11] X. Shen, et al., "A General Framework for Multi-Vehicle Cooperative Localization Using Pose Graph," arXiv:1704.01252, 2017.

[12] P. J. Besl and N. D. McKay, "A Method of Registration of 3-D Shapes," IEEE Trans. on Pattern Analysis and Machine Intelligence, vol. 14, no. 2, pp. 239–256, 1992.

[13] P. Biber and W. Strasser, "The Normal Distributions Transform: A New Approach to Laser Scan Matching," Proc. of IEEE/RSJ Int. Conf. on Intelligent Robots and Systems (IROS 2003), pp. 2743–2748, 2003.

[14] R. B. Rusu, N. Blodow, and M. Beetz, "Fast Point Feature Histograms (FPFH) for 3D Registration," Proc. of IEEE/RSJ Int. Conf. on Robotics and Automation, pp. 3212–3217, 2009.

[15] A. Aldoma, et. al., "Tutorial: Point Cloud Library: Three-Dimensional Object Recognition and 6 DoF Pose Estimation," IEEE Robotics & Automation Magazine, vol.19, issue 3, pp. 80–91, 2012.

[16] K. Inui, M. Morikawa, M. Hashimoto, and K. Takahashi, "Distortion Correction of Laser Scan Data from In-vehicle Laser Scanner based on Kalman Filter and NDT Scan Matching," Proc. of the 14th Int. Conf. on Informatics in Control, Automation and Robotics (ICINCO), pp. 329–334, 2017.

[17] K. Tokorodani, M. Hashimoto, Y. Aihara, and K. Takahashi, "Point-Cloud Mapping Using Lidar Mounted on Two-Wheeled Vehicle Based on NDT Scan Matching," Proc. of the 16th Int. Conf. on Informatics in Control, Automation and Robotics (ICINCO), pp.446–452, 2019.

[18] S. Kanaki, et al., "Cooperative Moving-Object Tracking with Multiple Mobile Sensor Nodes -Size and Posture Estimation of Moving Objects using In-vehicle Multilayer Laser Scanner-," Proc. of 2016 IEEE Int. Conf. on Industrial Technology (ICIT 2016), pp. 59–64, 2016.

[19] S. Tanaka, C. Koshiro, M. Yamaji, M. Hashimoto, and K. Takahashi, "Point Cloud Mapping and Merging in GNSS-Denied and Dynamic Environments Using Only Onboard Scanning LiDAR," Int. J. on Advances in Systems and Measurements, vol. 13 no. 3&4, pp. 275–288, 2020.

 ISBN: 978-1-61208-917-1

Development and Application of an Energy Harvesting Power Factor and Apparent Power Sensor

Takaya Yoshitake
Department of Communication Engineering and Informatics
The University of Electro-Communications
Chofu, Japan
Email: y2131168@edu.cc.uec.ac.jp

Shunkichi Takamatsu, Shinichiro Mito
Department of electronic engineering
National Institute of Technology, Tokyo College
Hachioji, Japan
Email: mito@tokyo-ct.ac.jp

***Abstract*— A contactless, wireless and battery-free alternating current (AC) apparent power and power factor sensor was developed. A current sensing transformer was not only used as a noncontact current sensor but also acted as a power supply for the sensor. The AC voltage waveform was measured without metal contacts using a piezoelectric film. A low-power circuit was designed to measure the power factor from the current and voltage waveforms. The data obtained from the developed sensor showed good agreement with the results from a commercially available power meter. The sensor developed in this work is expected to enable energy savings and carbon dioxide reduction in industrial applications.**

Keywords; electrical power; electric field; noncontact measurement; energy harvesting; SDG

I. INTRODUCTION

Reduction of electrical power consumption remains a constant issue in factories because it will not only reduce manufacturing costs but will also reduce CO2 emissions [1][2] and thus enable compliance with the International Organization for Standardization (ISO) 14001 standard [3]. To achieve the required reduction, it is important to measure the power consumption of each item of equipment precisely [4]. For this purpose, compact, easy-to-install, and inexpensive wireless power consumption sensors are required, but at present, there is no sensor available that can achieve all these demands [5]-[10]. Several nonmetallic contact methods for voltage waveform measurement have been proposed [11]-[14] that offer the advantages of ease of installation and non-invasive techniques. However, these proposed methods are expensive or require multiple probes that make them difficult to implement.

In this study, we propose a non-metal-contact voltage measurement method based on a single probe using a piezoelectric film. In addition, we have fabricated and evaluated an energy-harvesting, non-invasive, and retrofittable wireless power consumption sensor for factory use that consists of the proposed voltage sensor, a current transformer, an energy-harvesting circuit, a power-factor (PF) measurement circuit and a wireless communication module. The device does not require complex electrical work, and it will cost approximately $20 because of its simple design.

In Section 2, the block diagram of our sensor is presented. Section 3 describes the non-metal-contact voltage measurement process using the piezoelectric film. Section 4 presents the PF measurement circuit. Section 5 shows the results from field tests. Section 6 presents the conclusions drawn from this study.

II. CONFIGURATION OF THE SENSOR

The configuration of the developed sensor is shown in Figure 1. We used a current transformer to measure the current in a contact-free manner. The operating power of the wireless module can also be obtained from the current transformer. The sensor can be powered by energy harvesting. The apparent power was calculated by multiplying the assumed-to-be-constant voltage by the measured current. The PF was calculated using the phase difference between the voltage waveform acquired by the proposed voltage sensor and the current waveform. The apparent power and PF obtained were transmitted using the wireless module (TWE-Lite, Mono Wireless Inc., Kanagawa, Japan).

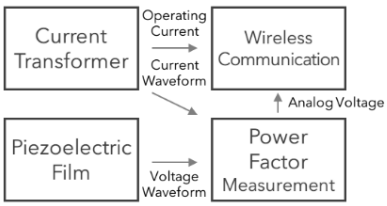

Figure 1. Block diagram of the PF and apparent power sensor

Installation of the developed sensor is easy because noncontact single probes are used for both the current and voltage measurements. Furthermore, our sensor requires much less maintenance than conventional sensors because of its energy harvesting-based operation.

III. NON-METAL-CONTACT VOLTAGE MEASUREMENT USING PIEZOELECTRIC FILM

A voltage can be measured non-invasively using a single probe by measuring the electric field strength around a wire when the voltage is applied to the wire [11][12]. We have focused on use of a piezoelectric film to provide a low-cost method to measure electric fields. The piezoelectric film comprises a piezoelectric material sandwiched between metal

 ISBN: 978-1-61208-917-1

electrodes. The piezoelectric material is polarized by the electric field around the wire, and a potential difference is then generated between the two electrodes. The electric field around the wire can thus be detected using a single piezoelectric probe.

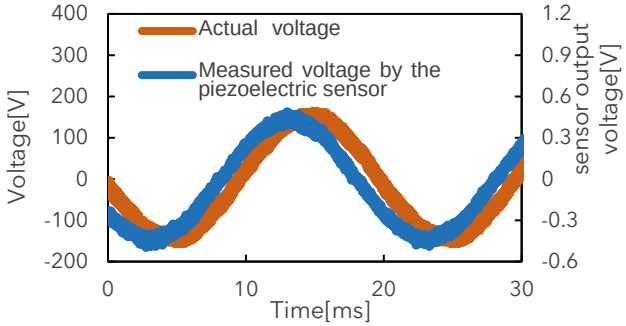

Figure 2. Results of noncontact voltage measurements using the piezoelectric film

A commercially-available piezoelectric film (LDT0-028K, TE Connectivity, Schaffhausen, Switzerland) was bent and was placed at a uniform distance from the center of the wire. The observed voltage waveform is shown in Figure 2. Although the output voltage and phase varied depending on the distance between the piezoelectric film and the wire, the correlation coefficient obtained for the actual and measured waveforms was 0.99. The proposed method can measure the relative change in the voltage, which is sufficient to enable calculation of the PF. The piezoelectric sensor output was related in advance to the actual voltage and was consistent with the calculation results from the equivalent circuit.

IV. POWER FACTOR MEASUREMENT CIRCUIT

The developed sensor was operated using the power obtained from the current transformer; it is thus necessary to measure the PF with low power consumption. In this research, we used an analog circuit to perform PF measurements with low power consumption.

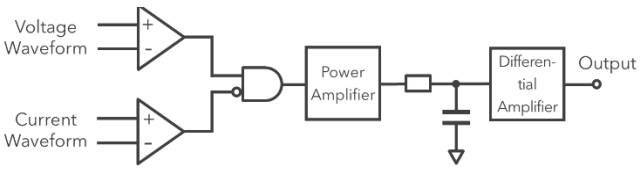

Figure 3. Block diagram of PF measurement circuit.

Figure 3 shows the block diagram of the fabricated PF measurement circuit. The current and voltage waveforms are converted into square waves, and the phase difference is then obtained as the pulse width by taking the logical product of these waves. Subsequently, the phase difference is output as an analog voltage through power amplification, smoothing, and differential amplification processes. The output is connected to the analog-to-digital converter of the wireless module and the data are transmitted. This circuit can be applied to both single- and three-phase electrical loads.

V. FABRICATION AND FIELD TEST

The noncontact wireless apparent power and PF sensor was fabricated as shown in Figure 4. The fabricated sensor was then attached to an injection molding machine (SH100C, Sumitomo Heavy Industries, Tokyo, Japan) for field testing.

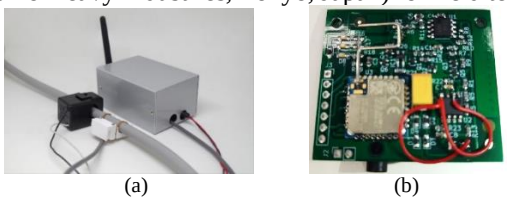

(a) (b)

Figure 4. Fabricated sensor. (a) Appearance of the fabricated sensor. The black probe is the current transformer, and the white probe is the voltage probe developed in this work. The silver box contains the processing circuit. (b) Appearance of the fabricated sensor board.

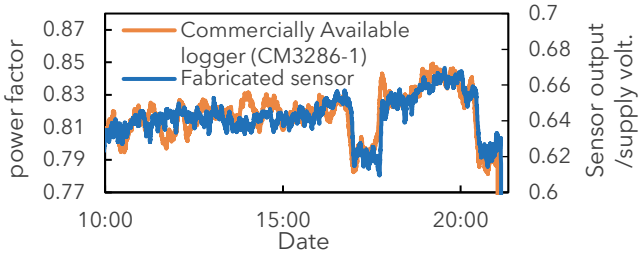

Figure 5. Comparison of the PFs obtained from a commercially available logger and the fabricated sensor.

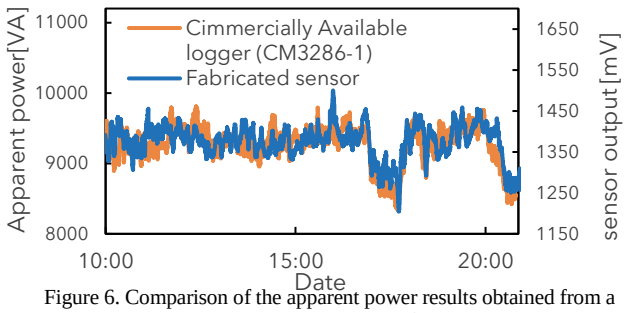

Figure 6. Comparison of the apparent power results obtained from a commercially available logger and the fabricated sensor.

Figures 5 and 6 show comparisons of the PFs and the apparent power values, respectively, that were measured using the developed sensor with those measured using a commercially-available power logger (CM3286-01, HIOKI E.E., Tokyo, Japan). The PF obtained by the developed sensor has a correlation coefficient of 0.80 with that measured using the commercial logger. The apparent power showed a correlation coefficient of 0.73. These results indicate that our sensor was able to measure the power consumption sufficiently accurately. The accuracy is suitable for rough logging of the PF and could be improved by calibration and grounding processes.

VI. CONCLUSION

Voltage waveforms have been measured using a single piezoelectric probe without metal contacts. An energy-harvesting wireless apparent power and PF sensor was prototyped using this piezoelectric probe. The data acquired using the developed sensor showed good agreement with the data acquired using a commercially-available power meter.

 ISBN: 978-1-61208-917-1

ACKNOWLEDGMENT

This research is supported by the Adaptable and Seamless Technology Transfer Program (A-STEP) JPMJTM20M3 from the Japan Science and Technology Agency (JST). We thank David MacDonald, MSc, from Edanz (https://jp.edanz.com/ac) for editing a draft of this manuscript.

REFERENCES

[1] A. Hawkes, "Estimating marginal CO2emissions rates for national electricity systems," Energy Policy, vol. 38, pp. 5977-5987, 2010.

[2] T. Unger , and E. O. Ahlgren, "Impacts of a common green certificate market on electricity andCO2-emission markets in the Nordic countries," Energy Policy, vol. 33, pp. 2152-2163, 2005

[3] P. Gupta, "End of life considerations for EV batteries - ISO and Indian business perspectives," 6th Hybrid and Electric Vehicles Conference (HEVC 2016), 2016, pp. 1-5, doi: 10.1049/cp.2016.0989.

[4] W. Gans, A. Alberini , and A. Longo, "Smart meter devices and the effect of feedback on residential electricityconsumption: Evidence from a natural experiment in Northern Ireland," Energy Economics, vol. 36, pp. 729-743, 2013.

[5] B. K. Barman, S. N. Yadav, S. Kumar , and S. Gope, "IOT Based Smart Energy Meter for Efficient Energy Utilization in Smart Grid," 2018 2nd International Conference on Power, Energy and Environment: Towards Smart Technology (ICEPE), 2018, pp. 1-5, doi: 10.1109/EPETSG.2018.8658501.

[6] T. Sirojan, S. Lu, B. T. Phung , and E. Ambikairajah, "Embedded Edge Computing for Real-time Smart Meter Data Analytics," 2019 International Conference on Smart Energy Systems and Technologies (SEST), 2019, pp. 1-5, doi: 10.1109/SEST.2019.8849012.

[7] P. Kumar , and U. C. Pati, "IoT based monitoring and control of appliances for smart home," 2016 IEEE International Conference on Recent Trends in Electronics, Information & Communication Technology (RTEICT), 2016, pp. 1145-1150, doi: 10.1109/RTEICT.2016.7808011.

[8] A. S. Musleh, M. Debouza , and M. Farook, "Design and implementation of smart plug: An Internet of Things (IoT) approach," 2017 International Conference on Electrical and Computing Technologies and Applications (ICECTA), 2017, pp. 1-4, doi: 10.1109/ICECTA.2017.8252033.

[9] W. Hlaing et al., "Implementation of WiFi-based single phase smart meter for Internet of Things (IoT)," 2017 International Electrical Engineering Congress (iEECON), 2017, pp. 1-4, doi: 10.1109/IEECON.2017.8075793.

[10] Chien-Hsun Huang, Tung-Tsun Hsien , and Gwo-Jia Jong, "Indoor power meter combined wireless sensor network for smart grid application," 2012 8th International Conference on Information Science and Digital Content Technology (ICIDT2012), 2012, pp. 336-339.

[11] D. Onishi et al., "Surface potential measurement of stress grading system of high voltage rotating machine coils using pockels field sensor," 2017 International Symposium on Electrical Insulating Materials (ISEIM), 2017, pp. 95-98, doi: 10.23919/ISEIM.2017.8088697.

[12] C. Peng, P. Yang, X. Wen, D. Fang , and S. Xia, "Design of a novel micromachined non-contact resonant voltage sensor for power distribution systems," SENSORS, 2014 IEEE, 2014, pp. 978-981, doi: 10.1109/ICSENS.2014.6985166.

[13] A. Rodriguez-Garde, A. B. Socorro-Leranoz, M. E. Martinez, J. Goicoechea , and I. R. Matias, "Dynamic Response of Gold-coated Optical Fiber Sensors Subjected to Voltage Variations," 2020 IEEE SENSORS, 2020, pp. 1-4, doi: 10.1109/SENSORS47125.2020.9278838.

[14] P. S. Shenil, R. Arjun , and B. George, "Feasibility study of a non-contact AC voltage measurement system," 2015 IEEE International Instrumentation and Measurement Technology Conference (I2MTC) Proceedings, 2015, pp. 399-404, doi: 10.1109/I2MTC.2015.7151301.

 ISBN: 978-1-61208-917-1

Recent Advances in IoT-Based Wearable Systems for Biosignals Monitoring – Application to Elderly Care

Emmanouel T. Michailidis, Panagiotis Pikasis, and Grigoris Kaltsas
microSENSES Laboratory, Department of Electrical and Electronics Engineering, University of West Attica, Ancient Olive-Grove Campus, 12243 Athens, Greece
e-mail: emichail@uniwa.gr, mscres-1@uniwa.gr, G.Kaltsas@uniwa.gr

***Abstract*—The evolution of the Internet of Things (IoT) ecosystem has been based on the advances of miniaturized, cheap, but powerful wearable sensors that can be used in various applications, including the real-time monitoring of elderly people's health condition. The sensing capabilities of wearable devices along with the communication capabilities offered by sophisticated wireless techniques and protocols intend to improve the quality of elderly people's life. This paper aims to review recent research work on sensor deployments and wearable technologies for biosignals monitoring for elderly care. Emphasis is also given on the advanced wireless technologies that are used for relevant healthcare IoT applications.**

Keywords-Communication protocols; elderly people monitoring; Internet of Things (IoT); wearables; Wireless Sensor Network (WSN).

I. INTRODUCTION

In recent years, the number of smart devices, wireless technologies, networking protocols, and wearables has rapidly increased and the Internet of Things (IoT) has emerged as a key enabler for the provision of challenging healthcare applications [1]. As the healthcare IoT will significantly affect the IoT-driven healthcare industry, the wearable technology has been widely adopted by the scientific community [2], in order to fabricate assisting devices that focus on various categories, such as elderly people, athletes, workout users, workers, and patients.

The wearable systems contain non-invasive sensors, which are used to measure physiological or biomechanical signs and strongly support welfare and critical healthcare IoT applications for elderly people [3], [4]. Typical examples of these sensors are bioelectric sensors (e.g., Electrocardiography (ECG), Photoplethysmography (PPG), Electromyography (EMG)), acoustical sensors (e.g., microphones) mechanical sensors (e.g., accelerometer gyroscope), chemical sensors (e.g., PH, perspiration), and thermal sensors (e.g., thermistor). Various physiological information can be extracted from biosensors analysis. Specifically, skin temperature, blood pressure, heart rate, respiration rate, and oxygen saturation are some of the parameters that can be determined.

On the other hand, wearable monitoring systems and IoT have been directly linked to wireless communication technologies [5], [6], which enable the data interaction of devices worn by elderly people in real time with other proximate or remote wireless nodes, thus creating Wireless Sensor Networks (WSNs) that collect physical data (e.g., body temperature, blood pressure, heart rate, oxygen saturation (SpO_2), and ECG). More importantly, adoption of advanced communication technologies facilitates the efficient, flexible, and cost-effective data collection from biomedical sensors and then the transmission of health data to central IoT nodes. Using wireless communication protocols, elderly people's vital signals can be remotely monitored [7] and aging population can be served by medical diagnosis and telemonitoring via IoT-powered In-Home Healthcare (IHH). Moreover, medical personnel and patients can interact though videoconferencing, whereas real-time medical imaging and remote robotic surgery are viable by exploiting high bandwidth wireless communication links.

Motivated by the aforementioned observations, this paper focuses on shedding light on recent advances on IoT-based wearable systems for biosignals monitoring of elderly people in a remote manner. In this direction, wearable healthcare devices, sensors deployments and various IoT based bio-monitoring systems are reviewed, mainly focusing on the field of elderly care. In addition, relevant communications technologies and wireless standards that can be used in healthcare monitoring applications are described and the main open issues in the field are underlined.

The rest of the paper is organized as follows. Section II describes recent advances on wearable systems and devices, followed by a presentation on their application on elderly care. Section III presents the advanced wireless technologies that intend to enrich the capabilities of IoT-based wearable systems for biosignals monitoring. Finally, conclusions and future research directions are drawn in Section IV.

II. IOT WEARABLE SYSTEMS FOR BIOSIGNALS MONITORING

Recently, new sensing elements came up in biosensing technology and monitoring of vital signs through wearable systems to predict the physiological state of elderly people. In [8], a system that can store and monitor vital signs was demonstrated. This system ('Abuelometro') was used in an elderly care facility to help caregiving staff monitor elderly residents. Moreover, a biometric wearable device from Hexiwear was used in [9], capable of measuring skin temperature, oxygen saturation, and heart rate. Based, on this device, a platform was fabricated that storage vital signs with extra information, such as exercise time, sleep time eat time, etc. In addition, an abnormal condition detection system was proposed in [10] with the aim of helping the elderly. The

 ISBN: 978-1-61208-917-1

system observed ECG, triaxial acceleration and skin temperature featured in a wireless wearable biosensor developed by Medical electronics Science Institute (MESI). The device communicated with a personal computer (PC) and the corresponding data was analyzed by a custom-made software. In case of abnormal conditions being detected, caregivers and relatives were notified by email. The ECG circular pads had to be placed near the heart, in order to determine heart rate with the required precision. The embedded triaxial accelerometer was used to examine body position. Also, fall detection algorithms that analyze accelerometer measurements were responsible for alerting users in an abnormal fall case.

In [11], a device that can monitor vital signs in real time was fabricated. The sensor device included an optical sensor using the Photoplethysmography (PPG) method, in order to monitor the blood change of the vessels [12], as well as a printed Radio Frequency (RF) antenna. The communication protocol used was the Mi-Wi. All data derived from the sensors, travel through the gateway to the smartphone app and are uploaded to the cloud. Furthermore, in [13], a wearable device was implemented that was able to record blood pressure via ECG electrodes along with body and environmental temperature. Both measurements were transmitted wirelessly using a Bluetooth module. By processing the measured data various parameters were extracted, such as heart rate, breath frequency, blood pressure, air, and skin temperature. Additionally, hand and arm movements could be determined by the accelerometer response. In [14], a system capable of monitoring vital signs and alerting caregivers in case of an emergency was presented in [14]. This system consists of a health watch with an attached optical sensor for PPG measurements, smart clothes (vest) constructed of conductive fiber, in order to collect the ECG signals and a body tag, incorporating a 3-axis accelerometer and gyroscope for body movements monitoring. Moreover, this system can communicate through a Bluetooth Low Energy (BLE) to Wi-Fi gateway and send the raw data from sensors to cloud. The system can provide daily data on user sleep quality, heart rate, change in blood oxygen concentration change, and walking steps.

An optical cuffless PPG sensor was fabricated in [15], in order to continuously monitor blood pressure and heart rate in real time consists of a Light-Dependent Resistor (LDR) and a circuit with a Light Emitting Diode (LED) enclosed in an elastic material held to the user's finger by Velcro. The device achieved an accuracy of 5% in the determination of real arterial blood pressure. In [16] a vital signs collector and a wearable device called "smart clothing" were proposed. More specifically, a T-shirt with embedded a Negative Temperature Coefficient (NTC) thermistor for temperature monitoring was fabricated. In addition, an optical sensor was used to capture oxygen saturation, whereas an ECG sensor was used to measure the heart rate using dry textile dry electrodes. Additionally, using Machine Learning (ML), the ECG signals were analyzed, in order to emotionally detect the user's mood. In [17], the SMARTA project was demonstrated. This project developed and tested a personal health system by integrating environmental sensors and wearable devices, in order to telemonitor vital signs and detect anomalies. In this regard, a wearable with an ECG sensor and an accelerometer was used that could monitor arterial pressure, oxygen saturation, and detect anomaly cases (e.g., user fall, immobility, etc.). Also, a wearable device for the purpose of monitoring the elderly people was presented in [18]. This device could be worn by the individual to collect physical activity data in a memory card. An accelerometer, a gyroscope and a heart rate sensor were used to track activities and vital signs. The heart rate device consisted of an acoustic sensor to pick up the beating sound of the heart. The device is worn in a belt and placed close to the heart. Figure 1 illustrates the aforementioned wearable devices, while Table I provides details about them.

III. Wireless Technologies for Biosignals Monitoring

In order to transmit the acquired information and obtain a reliable wireless connection between wearables and other IoT entities, various communication mechanisms can be implemented, such as Device-to-Device (D2D), device to human and vice versa, and device to distributed storage [6]. However, the wearables inherently have constraints in terms of computation, memory, energy, and operational cost. Thus, appropriate lightweight protocols (e.g., Constrained Application Protocol (CoAP), Message Queue Telemetry Transport (MQTT), and Extensible Messaging and Presence Protocol (XMPP)) have been adopted to enable the interaction among devices. On the other hand, signal attenuation, fading, and interference may affect signal propagation, whereas spectrum regulatory restrictions may exist. Thus, choosing the proper wireless technology and frequency band is of paramount importance. Generally, the local connectivity in IoT-based wearable systems is provided by means of a Wireless Local Area Network (WLAN) or short-range wireless networks, such as the Wireless Personal Area Network (WPAN). In this respect, one or multiple appropriate radio access technologies can be used, e.g., BLE, ZigBee, and IPv6 over Low-Power Wireless Personal Area Networks (6LoWPAN).

In recent years, various works have been various works adopting wireless technologies for biosignal monitoring. In [19], an Arduino-based deployment with Bluetooth capabilities for ECG measurement was described, whereas a low-cost and energy-efficient TI MSP430 microcontroller with a ZigBee/Bluetooth module was exploited in [20] to monitor heart rate, temperature, humidity and accelerometric data. Additionally, a Raspberry Pi was employed in [21] for remote elderly care and the health information was transferred using a WLAN or a PAN and a Bluetooth modem. Extended connectivity for measuring ECG, heart rate, body temperature and blood pressure was obtained in [22] using IEEE 802.11 Wi-Fi, Global Positioning System (GPS) and Radio-Frequency Identification (RFID) technologies along with the ThingSpeak IoT platform. In [23], a large number of patients was connected to the computer systems using a nRF24L01+ low power transceiver and the Enhanced ShockBurst protocol, whereas the measured data was visualized using the NI LabVIEW.

 ISBN: 978-1-61208-917-1

Several wireless technologies (i.e., 6LoWPAN, ZigBee, BLE) and protocols (i.e., CoAP and MQTT) were combined in [24] to obtain reliable sleep apnea diagnosis. In this respect, experiments were conducted and the results underlined that the 6LoWPAN protocol had the highest latency values, compared to ZigBee and Bluetooth.

As far as wearable systems are concerned, the WPANs are transformed into Wireless Body Area Network (WBANs), which have been recently evolved because of to the advances in microelectronics, System on Chip (SoC) design, and intelligent low-power sensors. By using WBANs consisting of in-body and on-body area networks, affordable and smart health care systems can be developed that support diagnostic procedures and the collection of sensitive and life-critical data without constraining the normal life of elderly people. To enable data transmission, the WBANs utilize the Wireless Medical Telemetry Services (WMTS), Ultra-wideband (UWB) and Medical Implant Communications Service (MICS) bands. Besides, the licensed Medical Implant Communication System (MICS) band (402-405 MHz) can be used for implant communications, whereas the wireless standard IEEE 802.15.6 represents the international standard for WBAN. A monitoring system for elderly care was implemented in [25] using a Zigbee-based Body Sensor Network (BSN) as well as the patients' smartphones to store and send the measured health information to remote servers.

On another front, long-range wireless connectivity can be achieved using conventional, i.e., Fourth Generation (4G) and Fifth Generation (5G) cellular networks, satellite networks, and Low-Power Wide Area Network (LPWAN) technologies, e.g., Long Range (LoRa), Sigfox, and Narrowband-IoT (NB-IoT). A Global System for Mobile Communications (GSM)/GPS-based module was utilized in [26] to enable mobile monitoring and attribute in real-time the stress levels of patients by measuring the heart rate, skin resistance and body temperature. Moreover, a cost-effective IoT system and a LoRa-based gateway were used in [27] to monitor the health condition of elderly people located in their residence, thus improving their quality of life. Also, the combination of LoRa and the MQTT protocol was studied in [28]. Figure 2 depicts wireless technologies for ubiquitous health and activity monitoring of elderly people. Although current technologies can facilitate the provision of healthcare IoT services, there are several issues that require further investigation, such as mobility, heterogeneity, interoperability, scalability, security, and privacy.

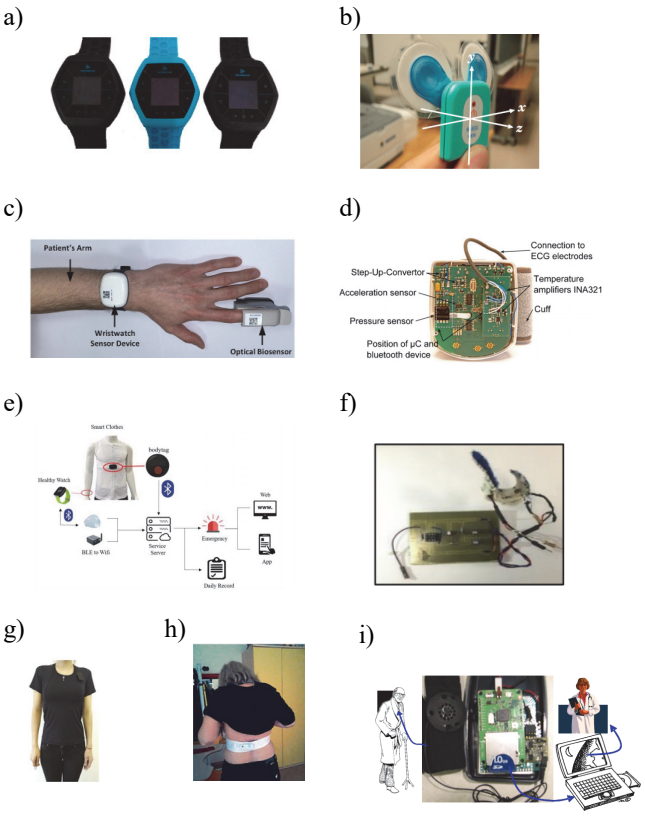

Figure 1. A simple representation of the described wearable devices a) [8] b) [10] c) [11] d) [13] e[14] f) [15] g) [16] h) [17] i) [18]

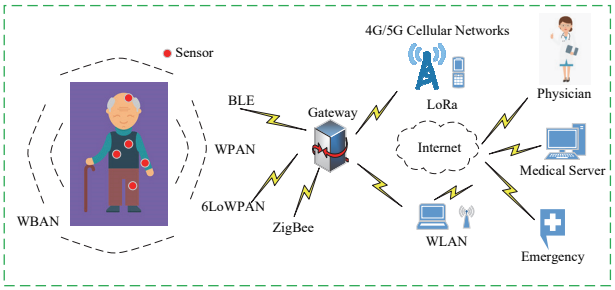

Figure 2. A simple representation of a wearable sensor network and relevant short-range and long-range wireless communication technologies for biosignals monitoring of elderly people.

TABLE I
DEVICES FOR IOT-BASED WEARABLE SYSTEMS

Ref.	Sensors	Monitoring Parameter	Housing	Communication Protocol
[8]	PPG optical sensors, temp. sensor	body temperature, oxygen saturation	strap	BLE
[10]	ECG electrodes temp. sensor	body temperature, heart rate	suction cup	USB
[11]	PPG optical sensor	pressure, heart rate, oxygen saturation	strap	Mi-Wi
[13]	ECG electrodes, temp. sensor	blood pressure, body temperature	Cuff	Bluetooth
[14]	PPG optical sensor, ECG electrodes	heart rate, oxygen saturation	vest	BLE
[15]	PPG optical sensor	blood pressure, heart rate	finger Velcro	Bluetooth
[16]	PPG optical sensor, ECG dry textile electrodes, thermistor	blood pressure, skin temperature, oxygen saturation	T-shirt	Bluetooth
[17]	ECG electrodes	blood pressure, oxygen saturation	belt- patch	BLE
[18]	Acoustic sensor	heart rate	belt	memory card

 ISBN: 978-1-61208-917-1

IV. Conclusion and Future Work

In this paper, the role of advanced wearables and wireless technologies in the IoT-based biosignals monitoring area for effective elderly care has been described. Additionally, the system implementation of various wearable devices was presented, including the sensors, measurement techniques, vital signs detection methods, communication process, and fabrication forms. Since reliable and ubiquitous short- and long-range connectivity is required, both conventional and low-power wireless technologies can drastically change the landscape of medical industries and strongly support the evolution of IoT-based wearable systems.

Evolution of IoT and biosensors will radically change the perspective of wearables usage as a major tool for biosignals monitoring. Thus, aiming to foster more developments towards implementing advanced wearables, further work should be conducted in the future. An interesting research area stands for the application of ML algorithms to accurately predict risk and dangerous or harmful situations for elderly people. Also, jointly adopting D2D and Mobile Edge Computing (MEC) to enhance the computation capacity of the network is also envisioned.

References

[1] M. A. Akkaş, R. Sokullu, H. Ertürk Çetin, "Healthcare and patient monitoring using IoT," *Internet of Things*, vol. 11, 2020, 100173.

[2] R. De Fazio, M. De Vittorio, and P. Visconti, "Innovative IoT Solutions and Wearable Sensing Systems for Monitoring Human Biophysical Parameters: A Review," *Electronics*, vol. 10, no. 14, p. 1660, Jul. 2021.

[3] T. G. Stavropoulos, A. Papastergiou, L. Mpaltadoros, S. Nikolopoulos, and I. Kompatsiaris, "IoT Wearable Sensors and Devices in Elderly Care: A Literature Review," *Sensors*, vol. 20, no. 10, p. 2826, May 2020.

[4] L. A. Durán-Vega, et al., "An IoT System for Remote Health Monitoring in Elderly Adults through a Wearable Device and Mobile Application," *Geriatrics*, vol. 4, no. 2, p. 34, May 2019.

[5] D. G. Kogias, E. T. Michailidis, S. M. Potirakis, and S. Vassiliadis, "Communication Protocols for Vital Signs Sensors Used for the Monitoring of Athletes," in V. Koncar, *Smart Textiles and their Applications*, Elsevier, 2016.

[6] D. G. Kogias, E. T. Michailidis, G. Tuna, and V. C. Gungor, "Realizing the Wireless Technology in Internet of Things (IoT)," in K. V. Arya, R. S. Bhadoria, and N. S. Chaudhari, *Emerging Wireless Communication & Network Technologies: Principle, Paradigm and Performance*, Springer, 2018.

[7] Al-khafajiy, et al., "Remote health monitoring of elderly through wearable sensors," *Multimedia Tools and Applications*, vol. 78, pp. 24681–24706, 2019.

[8] L. A. Durán-Vega, et al., "An IoT System for Remote Health Monitoring in Elderly Adults through a Wearable Device and Mobile Application," *Geriatrics*, vol. 4, no. 2, p. 34, May 2019.

[9] Hexiwear Complete IOT Development Solution. https://www.mikroe.com/hexiwear (accessed on 17 Oct. 2021).

[10] S. Yazaki and T. Matsunaga, "A proposal of abnormal condition detection system for elderly people using wireless wearable biosensor," in *Proc. 47th Annual Conference of the Society of Instrument and Control Engineers (SICE) of Japan*, pp. 2234-2238, 2008.

[11] S. Kumar, et al., "A Wristwatch-Based Wireless Sensor Platform for IoT Health Monitoring Applications," *Sensors*, vol. 20, no. 6, p. 1675, Mar. 2020.

[12] S. Chatterjee and P. Kyriacou, "Monte Carlo Analysis of Optical Interactions in Reflectance and Transmittance Finger Photoplethysmography," *Sensors*, vol. 19, no. 4, p. 789, Feb. 2019.

[13] T. Klingeberg and M. Schilling, "Mobile wearable device for long term monitoring of vital signs," *Computer Methods and Programs in Biomedicine*, vol. 106, no. 2, pp. 89-96, May 2012.

[14] P. Huang, C. Lin, Y. Wang and H. Hsieh, "Development of Health Care System Based on Wearable Devices," in *Proc. Prognostics and System Health Management Conference (PHM-Paris)*, Paris, France, pp. 249-252, 2019.

[15] Z. Cohen and S. Haxha, "Optical-Based Sensor Prototype for Continuous Monitoring of the Blood Pressure," *IEEE Sensors Journal*, vol. 17, no. 13, pp. 4258-4268, Jul. 2017.

[16] L. Hu, J. Yang, M. Chen, Y. Qian, and J. P. C. Rodrigues, "SCAI-SVSC: Smart clothing for effective interaction with a sustainable vital sign collection" *Future Generation Computer Systems*, vol. 86, pp. 329-338, Sep. 2018.

[17] L. Pigini, et al., "Pilot Test of a New Personal Health System Integrating Environmental and Wearable Sensors for Telemonitoring and Care of Elderly People at Home (SMARTA Project)," *Gerontology*, vol. 63, no. 3, pp. 281-286, 2017.

[18] A. Dinh, et al., "A Wearable Device for Physical Activity Monitoring With Built-in Heart Rate Variability," in *Proc. 3rd Int. Conf. on Bioinformatics and Biomedical Engineering*, pp. 1-4, 2009.

[19] B. Apsara, S. Bashyam, and B. Ramachandran, "Development of Low Power Wearable Physiological Signal Monitoring System", in *Proc. Int. Conf. on Nextgen Electronic Technologies: Silicon to Software*, Chennai, India, pp. 92-96, 2017.

[20] S. Warbhe and S. Karmore, "Wearable Healthcare monitoring system: A survey," in *Proc. 2nd Int. Conf. on Electronics and Communication Systems (ICECS)*, Coimbatore, India, pp.1302-1305, 26-27 Feb. 2015.

[21] F. Luna-Perejón, L. Muñoz-Saavedra, J. M. Castellano-Domínguez, and M. Domínguez-Morales, "IoT garment for remote elderly care network, *Biomedical Signal Processing and Control*," vol. 69, 2021, 102848.

[22] F. Shanin, et al., "Portable and Centralised E-Health Record System for Patient Monitoring Using Internet of Things (IoT)", in *Proc. Int. CET Conf. on Control, Communication, and Computing (IC4)*, Thiruvananthapuram, India, pp. 165-170, 5-7 Jul. 2018.

[23] E. Baba, A. Jilbab, and A. Hammouch, "A Health Remote Monitoring Application based on Wireless Body Area Networks," in *Proc. Int. Conf. on Intelligent Systems and Computer Vision (ISCV),* Fez, Morocco, 2-4 Apr. 2018.

[24] D. C. Yacchirema, D. Sarabia-JáCome, C. E. Palau, and M. Esteve, "A Smart System for Sleep Monitoring by Integrating IoT With Big Data Analytics," *IEEE Access*, vol. 6, pp. 35988-36001, Jun. 2018.

[25] M. S. H. Talpur, W. Liu, and G. Wang, "A ZigBee-based elderly health monitoring system: design and implementation," *International Journal of Autonomous and Adaptive Communications Systems (IJAACS),* vol. 7, no. 4, pp. 393-411, 2014.

[26] A. G. Airij, R. Sudirman, and U. U. Sheikh, "GSM and GPS based Real-Time Remote Physiological Signals Monitoring and Stress Levels Classification", in *Proc. 2nd Int. Conf. on BioSignal Analysis, Processing and Systems (ICBAPS)*, Kuching, Malaysia, 24-26 Jul. 2018.

[27] J. P. Lousado and S. Antunes, "Monitoring and Support for Elderly People Using LoRa Communication Technologies: IoT Concepts and Applications," *Future Internet*, vol. 12, no. 11, p. 206, Nov. 2020.

[28] A. Lachtar, T. Val, and A. Kachouri, "Elderly monitoring system in a smart city environment using LoRa and MQTT," *IET Wireless Sensor Systems*, vol. 10, no. 2, pp. 70-77, Apr. 2020.

 ISBN: 978-1-61208-917-1

On Exploring the Use of Mobility Parameters in the Analysis of Early Childhood Developmental Disorders

Rama Krishna Thelagathoti
College of Information Science and Technology
University of Nebraska Omaha
Omaha, NE 68182, USA
e-mail: rthelagathoti@unomaha.edu

Hesham H. Ali
College of Information Science and Technology
University of Nebraska Omaha
Omaha, NE 68182, USA
e-mail: hali@unomaha.edu

Abstract— **Impaired motor development is one of the initial signs of early childhood developmental disorders. Autism spectrum disorder (ASD), Cerebral Palsy (CP), and Attention Deficit Hyperactivity Disorder (ADHD) are the most common disorders that infants are affected in the USA. Albeit they are not being diagnosed until their school-age because there is no standardized clinical diagnosing routine like a blood test. Existing clinical diagnostic approaches are predominantly dependent on observational assessment by a trained physician along with patient feedback. Furthermore, these methods are subjective and do not provide an accurate decision. Nonetheless, research findings reveal that abnormal motor skills are often the initial signs of later developmental disorders. This paves the way for exploring alternative opportunities to identify the disease in the early stages of childhood. Recent advancements in sensing technologies facilitate convenient as well as unobtrusive methods to collect the mobility data even from the infants and be able to detect the disorder. Wearable devices are tiny and easy to use in collecting motor data from neonates and distinguish abnormal motor development from normal motor development. Thus, mobility data collection from an infant using a wearable sensor is beneficial in the early diagnosis of developmental disabilities like cerebral palsy. Our main contribution in this study is to present the analysis of various wearable sensor-based motor assessment methods in predicting childhood disorders. Furthermore, this document presents various crucial mobility parameters associated with identifying childhood disorders.**

Keywords- mobility; developmental disorder; wearable sensor;

I. INTRODUCTION

In recent years, the prevalence of developmental disorders among children is rising at an alarming rate. Early childhood developmental disorder is one of the primary causes for children being referred to primary healthcare clinics [1]. Chronic or perpetual delays in one or more motor functions of the child can be treated as a development disorder [2]. The onset of the disability may occur regardless of racial, ethnic, and socioeconomic groups. The manifestation of motor disability is caused by atypical brain development. Yet, specific reasons for atypical brain development are not known [3]. Research shows that preterm birth and pregnancy complications that occur in the perinatal period may affect the brain. Consequently, babies born in this category are at risk for neurodevelopmental impairments [4]. Additionally, low birth weight and infections during pregnancy are at high risk for several developmental disabilities. According to the study conducted by National Health Interview Survey (NHIS) in the United States, the growth of childhood disorders has increased to 17% between the years 2009 and 2017. Also, one out of six children between the age groups 3 and 17 years have one or more disabilities [6]. Furthermore, ADHD, ASD, and CP are the common disorders found among children and boys were more likely to be in the vulnerable group than girls [2].

The evolution of fine and gross motor skills in children with atypical neurodevelopment is cramped than children with typical neurodevelopment. As a result, affected children do not acquire smooth limb movements rather rigid and nonsynchronous [5]. Often, delays in acquiring sufficient motor movements are the early signs of later developmental impairment. Hence, an infant's motor assessment can be a potential parameter for the early diagnosis of the disability. Moreover, significant research is going on towards the assessment of an infant's motor function as a method to detect developmental disorders, such as cerebral palsy, autism [2][5][6]. The sooner the disorder is diagnosed the better the possibility for effective intervention therapy.

In the past decade, there has been a substantial rise in the quantitative assessment of motor dysfunction by attaching tiny sensors to neonates' upper and lower limbs. Abnormal movements are characterized by repetitive, stereotyped movements, rigid movements due to lack of smoothness, unusual gait patterns [4]. These atypical patterns are distinguishable by processing the mobility data collected from the sensors attached to a child's limb. Researchers have also concluded that abnormal movements are strongly correlated to their abnormal brain development [7]. The goal of motor assessment is to quantify the degree and range of motor disability and predict whether the child falls under the stage of Typical Development (TD) or At Risk (AR).

The primary purpose of this document is to review the various mobility assessment methods that were employed for diagnosing early childhood developmental disorders. At first subjective methods are discussed then wearable sensor-based assessment methods are elaborated. For this study, literature has been chosen which includes the following criteria.

1. The Data collected from human subjects by using wearable sensors
2. The primary aim of the article is to diagnose childhood disorders

 ISBN: 978-1-61208-917-1

3. The motor movements are the main diagnostic assessment
4. The fundamental human subjects are infants or preschool-age kids.

The remaining sections of the document are structured as follows. In Section II, qualitative assessment methods are discussed. Section III explains the types of devices used for mobility data collection. The quantitative diagnostic approaches are presented in section IV. Under Section V, various aspects of mobility-based assessment methods are elaborated. Finally, Section V concludes with a summary of this work.

II. BACKGROUND

To discuss different assessment methods following three generalized developmental stages are defined.

A. Developmental Stages

At Risk (AR): Neonates born preterm and with pregnancy complications are considered At Risk (AR) of developing aberrant motor function and eventually likely to be diagnosed with developmental disorders including CP [2].

Typically developing (TD): Infants with normal limb movements are classified as Typical Developing (TD) [2].

Neurodevelopmental disorder (NDD): children who are already diagnosed with any developmental disorders like CP, ASD, and ADHD are categorized as infants with NDD [8].

According to the CDC [2], a TD child reaches certain developmental milestones as they grow. For instance, a 12-month-old toddler should be able to sit without any help and exhibit variable movements. On the other hand, AR infants lag in acquiring one or more such skills.

B. Qualitative Assessment Methods

Traditional assessment is heavily dependent on visual observation by a trained physician. Sometimes physicians prepare a questionnaire and assess the level of abnormality by integrating the feedback from the parents and/or the child. In such a scenario, parents might unaware of specific symptoms that the child is suffering, and the child may not be able to give precise feedback as adults. Hence, the decision-making becomes more complex. Additionally, existing clinical methods, such as analysis of neuroimaging require a trained consultant physician. But reliability and accuracy are largely depending on the expertise of the consultant. Besides the inherent complexity in judging the presence of the disorder, estimating the severity of the illness is far more challenging. The inception of qualitative assessment of the infant's nervous system is indeed a breakthrough in the diagnosis of developmental disorders.

The Alberta Infant Motor Scale (AIMS) [9] is one of the early observational scales to assess the neonate's gross motor function. In this method, a rating will be calculated based on the infant's performance in weight-bearing, posture, and antigravity movements. This method can be used only for babies under 18 months of age and the observer needs extensive training in the respective assessment. Prechtl et al. [10] proposed another observation-based systematic methodology termed General Movement Assessment (GMA) for diagnosing cerebral palsy. They have postulated that the quality of General Movements (GMs) is cramped and lacks smoothness over time due to impaired brain development. The absence of GMs may be observed from the video recording of an infant. This approach also does necessitate training by experts. In another experiment [11], Heineman et al. developed a video-based mobility evaluation technique, the Infant Motor Profile (IMP), that can differentiate between kids between TD and AR neurodevelopment. The downside of all these methods is that it involves an enormous human effort to examine the video recording for accurate prediction. Melbourne Assessment of Unilateral Upper Limb Function-2 (MA-2) is a standard reference tool to measure the quality of upper limb movements in kids with atypical brain growth aged between 2 to 15 years [12]. Moreover, scoring is estimated based on how a child performs 14 test activities including pickup and release of some objects.

Nonetheless, rating-dependent approaches have various shortcomings. (1) assessment is entirely observer-dependent. consequently, there is a high probability that the observer will make a wrong estimation. (2) Evaluation is time-intensive and consumes immense human effort. (3) The observer is required to be trained in advance with the necessary skills to make an optimal conclusion. After the training, it takes substantial time to acquire proficiency in the diagnosis. (4) Patients must visit the physicians and laboratories frequently. (5) Often, laboratories must have a specialized environment and equip with expensive tools. (6) monitoring the rehabilitation of the affected infants is challenging as there is a dependency on the observer. (8). Children's attention span is very limited, and so they can easily get annoyed with cumbersome instructions. Hence, it is essential to have an observer-independent approach with the best accuracy.

III. DATA AND DEVICES

Characterizing the atypical motor movements including repetitive and stereotypical patterns is crucial in the early diagnosis of neurodevelopmental disease. A qualitative examination of neonate movements necessitates a special skill set and the outcome varies from observer to observer [13]. To fill the gap, sophisticated systems, such as stereo photogrammetric movement analysis, gaze-tracking devices, and 3D motion tracking with passive markers [14] were introduced. Yet, these methods require an expensive structured setup with many wires and sensors to monitor the baby's physical movements. Wearable technology made it possible to collect the movement data by attaching tiny sensors to the body parts of the infants without major disturbance.

In recent times, Inertial Measurement Units (IMUs), also known as inertial sensors have been increasingly explored by numerous researchers. Typical IMUs comprise of

 ISBN: 978-1-61208-917-1

accelerometer, gyroscope, and occasionally include a magnetometer. Nevertheless, many scholars have employed an accelerometer-based sensor to acquire infants' arm and leg movements [4][15][16]. Wearable instruments are suitable for monitoring the limb movements of infants because of their flexibility in sensor placement, adaptability, and power efficiency. Since the human subject is an infant, sensors are usually embedded in an appropriate peripheral, such as Leg warmers [7], wristwatches [17]. In some studies, skin-adhesive sensors have also been used [18]. Although the device has a variety of sensing technology, the aim is to collect the movement data unobtrusively without creating considerable discomfort to the babies. Therefore, wearable sensors are efficient for the objective assessment of children's movements. Fig. 1 depicts the convenient body locations where sensors are attached. And different impaired movements are shown that are characterized as aberrant motor movements exhibited by the disordered children.

Nowadays, wearable devices are compact yet affordable. They come with internal storage as well as a provision to connect and upload the data to cloud storage on the go. Most of the devices are battery-powered that eliminating the cumbersome wires and cables. When multiple sensors are included in the data collection process, then all the sensors must be actively synchronized throughout the duration. Then it allows collecting the data continuously from all the sensors even outside of the lab environment like home. Primarily, these devices are used to record upper and lower limbs that will help characterize the disorder.

IV. QUANTITATIVE ASSESSMENT

Measuring abnormality from the child's movements is an important clinical task as it reduces the significant human effort in identifying the impaired motor skills. Further, it helps physicians to come to an objective conclusion. With the latest advancements in wearable devices, it has become easy to attach them to infants and collect the data continuously. Various quantitative motor assessment studies are summarized in Table 1. This study includes the research that has employed wearable sensors and finds the quantitative measurement of the children's motor movements.

A few scholars had toiled and developed unobtrusive and non-invasive wearable instruments suitable for infants and toddlers. As early as 2008, Campolo et al. [14] prototyped a wearable sensing system for monitoring the upper and lower limb spontaneous movements of premature babies. Their sensing instrument can be used in infants as young as 2 weeks. They have hypothesized that abnormal movements are the early signs of later developmental disorders, such as autism. Redd et al. [18] carried a pilot project on a single healthy born infant to assess the General Movements (GMs) and Fidgety Movements (FMs) [10]. They have built a wearable monitoring system with an array of sensors to acquire the infant movements for both the short and long-term. Their results show that the absence of variability in GMs and FMs might be the early sign for the manifestation of neurodevelopmental disorders, such as CP. Nonetheless, they have experimented with only one healthy infant.

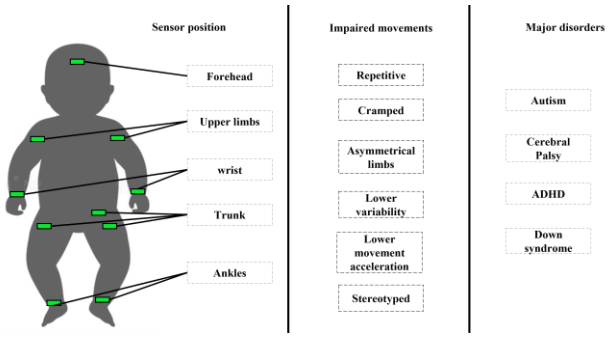

Figure 1: sensor-based quantitative diagnosis

Typically developing (TD) neonates demonstrate a rich and variable repertoire of movements compared to their counterpart infants at risk (AR) [19]. Often, it is critical to categorize between TD and AR during early infancy. Abrishami et al. [19] quantified infants' spontaneous leg movements by embedding tiny sensors inside custom-designed leg warmers. This study aimed to classify the group of infants into (TD) or (AR) from the day-long (8-13 hours) leg movements data. They also analyzed sensor data recorded from AR infants and were able to distinguish between AR babies with poor and good development. In [19], Goodfellow et al. developed binary classification algorithms to predict whether the child is TD or AR. In this approach, a group of 22 infants aged between 0 to 12 months was divided into two groups as 0-6 months and 6-12 months. Then, extracted two sets of features for each group and found a significant difference between TD and AR mobility data of 0-6 months than 6-12 months. Their findings prove the prominence of early childhood diagnosis.

Similarly, numerical estimation of abnormal mobility has also been studied in the past as it helps in distinguishing both, healthy and impaired. One of the early experiments demonstrated by Gravem et al. [4], utilized a simple accelerometer sensor and was able to collect the data from the premature neonates recruited from the NICU, who are potentially at risk of CP. Then, by extracting features and applying the machine learning technique including Decision Trees, he was able to recognize the abnormal movements namely Ccramped-Synchronized General Movements (CSGMs) [10]. According to Prechtl's assessment for CP [22], the presence of CSGM is an early marker for lateral developmental disorders. Wilson et al. [20], formulated Motion Complexity (MC) by measuring the variability from the infant's leg movement data. They conjectured that infants with lower MC are at risk (AR) of disabilities, such as ASD. Moreover, AR subjects compose lower motion complexity compared to TD subjects because their actions are repetitive and stereotyped. Smith et al. [15] proposed Sample Entropy (SampEn) as a function to measure the variation and repetition in kids' leg movements. Additionally, SampEn is lower for infants with developmental delays than normal infants. A different experiment carried by Hoyt et al. [17], assessed only upper limb movements and recommended two metrics: The Use

 ISBN: 978-1-61208-917-1

TABLE 1: SUMMARY OF QUANTITATIVE METHODS

Reference	Purpose	Sensor	Sensor placement	Wear time (in hours)	Setting	Disorder	Movement type	Subjects	Age (in months)
[7]	Classify TD and AR	IMU	Ankles	8-13	Natural	NA	Spontaneous leg movements	12 TD 19 AR	1-15
[14]	Early diagnosis	IMU	Wrist and ankles	NA	Clinical	ASD	Spontaneous leg and arm movements	NA	NA
[19]	Classify TD and AR	IMU	Ankles	8-13	Natural	NA	Spontaneous leg movements	12 TD 19 AR	1-16
[20]	Diagnose ASD	IMU	Ankles	8-12	Natural	ASD	Spontaneous leg movements	5	3-12
[21]	Diagnose CP	Accelerometer	Ankles and wrist	20 min	Clinical	CP	Spontaneous leg and arm movements	19 TD 4 AR	<10
[18]	Diagnosis CP	IMU	Forehead, ankles, and wrist	1 min	Clinical	CP	Spontaneous head, leg, and arm movements	1 TD	3-5
[22]	Quantify leg movements	Inertial sensor	Ankles	8-13	Natural	NA	Spontaneous leg movements	12 TD	1-12
[4]	Predict impaired motor activity	Accelerometer	Head, ankles, and wrist	1	Clinical	CP	Spontaneous head, leg and arm movements	10 AR	<3
[23]	Number of days required for assessment	IMU	Ankles	5 days	Natural	NA	Spontaneous leg movements	16 AR	2-14
[15]	Measure variability of movements	IMU	Ankles	8-13	Natural	NA	Spontaneous leg movements	11 TD 20 AR	6-9
[24]	Assess leg movements	accelerometer	Right ankle	48 hrs. x 4 times	Natural	DS	Spontaneous right leg movements	8 TD 8 AR	3-6
[16]	Predict motor disorder	Accelerometer and gyroscope	Trunk, upper and lower limbs	4	clinical	CP, stroke	Predefined body movements	4 AR	9-12 years
[17]	Clinical vs motor assessment	Accelerometer	wrist	75	Natural	CP	Spontaneous upper arm movements	26 TD 26 AR	1-17 years

Ratio (UR) to measure the quality of using both arms and the Mono Arm Use Index (MAUI) for quantifying intensity and frequency of each arm. Their results signify that UR and MAUI are lower for typically developing children and higher for the children at of developmental delays.

Furthermore, many scientists are interested in studies specific to a particular disorder like cerebral palsy (CP) and Down Syndrome (DS). McKay et al. [24] conducted a mobility assessment of a group of infants with DS and without DS. Using an activity monitor attached to the baby's right ankle measured leg activity and sleep patterns at 3,4,5, and 6 months. Their statistical analysis observed a significant group difference between the infants with DS and without DS with respective to their motor component. Strohrmann et al. [16] acquired mobility data from four children (2 of them diagnosed with Cerebral Palsy and 2 others with stroke) who are undergoing rehabilitation. In this work, they were invited to perform a set of predefined motor tasks and measured the progress of the rehabilitation therapy using extracted features including smoothness in the upper and lower limb movements, and coordination between both arms. In another study conducted by Heinze. et al. [21], proposed an objective assessment methodology to diagnose cerebral palsy from the spontaneous leg and arm movements of newborn babies. Their method is built on a decision tree classifier algorithm and achieved ~90% accuracy. Further, they have posited that their methodology can be easily adapted by the clinical practitioners and helps to monitor the progress of rehabilitation.

A different experiment performed by Deng et al. [23] assessed the motor behavior of neonates to determine the minimum number of days required to characterize the ideal daily leg movement patterns of children who are at risk of developmental disorders. They hypothesized that two days of leg movement data is sufficient to accurately predict developmental disorder among the infants at risk. Smith et al. [22] developed an algorithm to measure the full day leg activity and attempted to identify the relationship between the number of leg movements and the onset of walking. However, their test produced surprisingly unexplainable results as infants with a smaller number of leg movements began walking early than the babies with a greater number of leg movements.

V. DISCUSSION

This section presents the various aspects of mobility-based assessment approaches and discusses their merits as well as demerits.

 ISBN: 978-1-61208-917-1

A. Challenges in Data Collection

Infants motor assessment using wearable sensors have been increasing over the last decade because of its miniature size and wearability. Also, sensors can be attached to any part of the body and have the capability to work in a laboratory setting as well as in a home environment. Nonetheless, unlike adults collecting data from kids is not so easy for various reasons. (1) Preparing an infant for data collection is challenging because they are fragile and need utmost care. If it is a lab environment, then room temperature must be adjusted to the comfort of the child [21]. Additionally, the parent must ensure essential daily routines, such as breastfeeding and diapering. So, the child is ready and perform desired spontaneous movements (2) Children's behavior is unpredictable, so sensors may drop off or loosen which can eventually add noise in the data stream. For this reason, in a clinical setting or home environment, either a parent or a caregiver must always be present to take care of sensor positing during the data acquisition period [23][25]. (3) size and sensor placement are important to lessen the irritation to the child. From the ongoing research, it is evident that the average weight of each sensor ranges between 10 grams to 30 grams [7][17][18]. However, the sensor's positioning has limited choices as it needs to be placed on the arms and legs to measure the limb movements.

B. Wear Time

Although there is no evidence for precise sensor wear time required for accurate data analysis, numerous studies collect the data for more than one hour for an objective conclusion. As wearable technology is advancing, it is now possible that sensors can be placed in diversified products like leg warmers [7] which are comfortable for the infant. Hence, some scholars have embedded sensors in the form of socks, wristwatches and were able to collect the data for 2 to 5 days. Nonetheless, according to the study conducted by Deng et al. [23], two days of sensor data of infants is sufficient to differentiate between typical and atypical movements pattern. Yet, further investigations are necessary to minimize the wear time.

C. Accuracy and Validation

Accuracy validation of an infant's motor assessment method is crucial for decision-making in clinical research. Irrespective of the methodology used for the assessment, it is essential to compare the results with ground truth to measure the accuracy of the model. Researchers are primarily depending on two types of accuracy validation approaches for the context of an infant's motor assessment. Each method differs by ground truth. (1) In this approach, the sensor data collection procedure is video recorded such that normal and abnormal movements are annotated by experts. This annotated data is used as ground truth to validate the accuracy [7][15][16][17][22]. Undoubtedly, it is one of the popular and fastest methods used in many studies. (2) As an alternative, some investigators do the follow-up of the infant's health status after a few months to validate their inference, of those who were classified as high risk. In a study done by Wilson et al. [20], the authors assessed children's movement complexity pattern at 3,6, 9, and 12 months of age, however, follow-up was done at 18 and 36 months of age to validate their results.

D. Noise Elimination

Unfortunately, infant movement data recorded from the sensors is mostly accompanied by noise [22]. Especially, in the context of infants, the amount of noise-induced might be higher than normal. Because the daily routine of every child frequently changes between sleep, waking, and active states. Besides, a child might experience discomfort for unknown reasons. Then, either parent or caregiver must pacify the child to resume the data recording. Thus, the presence of noise is inevitable in children's movement data. Due to the effects of noise, movement assessment derived from the noisy sensor data is biased and inaccurate. To eliminate the noise from the movement data, investigators have employed different techniques. To eliminate outliers, preprocessing and normalization of the data are some of the popular approaches [11][16][22]. In this approach, raw data is normalized and standardized to align within either first or third quantiles. Alternatively, parents or caregivers to write down the activity log of any major change in movement [7][15]. For instance, the activity log records the sleep, wake, and play times of the child. This method helps to extract the data which is relevant and useful based on the activity log.

E. Quantifiable Parameters

Quantitative measurement has been used by several researchers for the automatic assessment of impaired motor function. In contrast, some researchers have developed a quantifiable metric that can measure the level of motor impairment. Their main objective is to quantify variability and repeatability of arm and leg movements as a unit that can be used to measure the degree of neuromotor control. Wilson et al. [20] proposed an objective metric called Motion Complexity (MC) from the full-day mobility data acquired from the sensors attached to both legs. MC is computed from the duration of movement, peak acceleration, and average acceleration during a movement. MC is essentially a measure of the variability of the recorded leg movements. Their experimental results demonstrate that two kids from the sample of five subjects, have lower MC scores than the other three kids and they later developed ASD. Sample Entropy (SampEn) is another quantitative measure introduced by smith et al. [15]. Their analysis proved that AR infants' SampEn values are significantly lesser than TD infants. Hence, SampEn may be a potential early marker to detect abnormal growth of neuromotor control. Hoyt et al. [17] computed two metrics from the sensor data of upper limb movements: Use Ratio (UR) and mono arm use index (MAUI). These two components measure the asymmetry between the two arms. They postulated that infants with neurodevelopmental deficits might not use both arms like normal children. Their study results corroborated their theory.

 ISBN: 978-1-61208-917-1

F. Spontaneous Movements vs Therapeutic Movements

While spontaneous movements are either leg or arm movements recorded during an infant's active playtime, therapeutic (pre-defined) movements are designed by researchers in collaboration with clinical expert physicians [16]. Pre-defined movements are straightforward to process because they are logged in a well-controlled lab environment and accurate movement is well known in advance. Whereas spontaneous movements require additional processing to extract useful features as well as suppress unnecessary noisy data [21][22]. Although pre-defined movements processing technique is simple to use, scholars are mostly interested in spontaneous physical movements. Because the treatment of spontaneous arm and leg movements is more practical and accurate.

VI. Conclusion and Future work

Developmental disorders such as autism hamper the typical behavior of a child. Consequently, they do not grow like a normal child. Thus, it is crucial to diagnose and begin the treatment as soon as early infancy. However, the most frequently used clinical method is ineffective in the early detection of the disorder. Quantitative measurement of disability using smart wearable devices speeds up the diagnosing process. This document highlighted the importance of quantitative prognosis and presented the various diagnostic approaches that are explored by the scientific community as a method of identifying the disorder by employing sensor devices.

References

[1]. K. A. I. Evensen, S. Sellæg, A.-C. Stræte, A. E. Hansen, and I. Meisingset, "Profile of children referred to primary health care physiotherapy: a longitudinal observational study in norway," BMC Health Services Research, vol. 21, no. 1, pp. 1–10, 2021.

[2]. Centers for Disease Control and Prevention, "Developmental disabilities," 2021, [Online; retrieved: October 2021]. Available from: https://www.cdc.gov/ncbddd/developmentaldisabilities/index.html

[3]. B. Zablotsky et al., "Prevalence and trends of developmental disabilities among children in the United States: 2009–2017," Pediatrics, vol. 144, no. 4, e20190811,2019.

[4]. D. Gravem et al., "Assessment of infant movement with a compact wireless accelerometer system," Journal of Medical Devices, vol. 6, no. 2, 2012.

[5]. F. Ferrari et al., "Cramped synchronized general movements in preterm infants as an early marker for cerebral palsy," Archives of pediatrics & adolescent medicine, vol. 156, no. 5, pp. 460– 467, 2002.

[6]. L. Meinecke et al., "Movement analysis in the early detection of newborns at risk for developing spasticity due to infantile cerebral palsy," Human movement science, vol. 25, no. 2, pp. 125–144, 2006.

[7]. M. S. Abrishami et al., "Identification of developmental delay in infants using wearable sensors: Full-day leg movement statistical feature analysis," IEEE journal of translational engineering in health and medicine, vol. 7, pp. 1–7, 2019.

[8]. I. Braito et al.,"Assessment of upper limb use in children with typical development and neurodevelopmental disorders by inertial sensors: a systematic review," Journal of neuroengineering and rehabilitation, vol. 15, no. 1, pp. 1–18, 2018.

[9]. M. C. Piper, L. E. Pinnell, J. Darrah, T. Maguire, and P. J. Byrne, "Construction and validation of the alberta infant motor scale (aims)." Canadian journal of public health= Revue canadienne de sante publique, vol. 83, pp. S46–50, 1992.

[10]. C. Einspieler and H. F. Prechtl, "Prechtl's assessment of general movements: a diagnostic tool for the functional assessment of the young nervous system," Mental retardation and developmental disabilities research reviews, vol. 11, no. 1, pp. 61–67, 2005.

[11]. K. R. Heineman, A. F. Bos, and M. Hadders-Algra, "The infant motor profile: a standardized and qualitative method to assess motor behaviour in infancy," Developmental Medicine & Child Neurology, vol. 50, no. 4, pp. 275–282, 2008.

[12]. M. Randall, C. Imms, and L. Carey, "Establishing validity of a modified melbourne assessment for children ages 2 to 4 years," American Journal of Occupational Therapy, vol. 62, no. 4, pp. 373–383, 2008.

[13]. H. Chen, M. Xue, Z. Mei, S. Bambang Oetomo, and W. Chen, "A review of wearable sensor systems for monitoring body movements of neonates," Sensors, vol. 16, no. 12, p. 2134, 2016.

[14]. D. Campolo et al., "A novel technological approach towards the early diagnosis of neurodevelopmental disorders," in 2008 30th Annual International Conference of the IEEE Engineering in Medicine and Biology Society. IEEE, 2008, pp. 4875–4878.

[15]. B. A. Smith, D. L. Vanderbilt, B. Applequist, and A. Kyvelidou,"Sample entropy identifies differences in spontaneous leg movement behavior between infants with typical development and infants at risk of developmental delay," Technologies, vol. 5, no. 3, p. 55, 2017.

[16]. C. Strohrmann et al., "Monitoring motor capacity changes of children during rehabilitation using body-worn sensors," Journal of neuroengineering and rehabilitation, vol. 10, no. 1, pp. 1–16, 2013.

[17]. C. R. Hoyt et al.,"Using accelerometry for measurement of motor behavior in children: Relationship of real-world movement to standardized evaluation," Research in developmental disabilities, vol. 96, p. 103546, 2020.

[18]. C. B. Redd, L. A. Barber, R. N. Boyd, M. Varnfield, and M. K.Karunanithi, "Development of a wearable sensor network for quantification of infant general movements for the diagnosis of cerebral palsy," in 2019 41st Annual International Conference of the IEEE Engineering in Medicine and Biology Society (EMBC). IEEE, 2019, pp. 7134–7139.

[19]. D. Goodfellow et al., "Predicting infant motor development status using day long movement data from wearable sensors," arXiv preprint arXiv:1807.02617, 2018.

[20]. R. B. Wilson, S. Vangala, D. Elashoff, T. Safari, and B. A. Smith, "Using wearable sensor technology to measure motion complexity in infants at high familial risk for autism spectrum disorder," Sensors, vol. 21, no. 2, p. 616, 2021.

[21]. F. Heinze et al., "Movement analysis by accelerometry of newborns and infants for the early detection of movement disorders due to infantile cerebral palsy," Medical &

 ISBN: 978-1-61208-917-1

biological engineering & computing, vol. 48, no. 8, pp. 765–772, 2010.

[22]. B. A. Smith, I. A. Trujillo-Priego, C. J. Lane, J. M. Finley, and F. B. Horak, "Daily quantity of infant leg movement: wearable sensor algorithm and relationship to walking onset," Sensors, vol. 15, no. 8, pp. 19 006–19 020, 2015.

[23]. W. Deng, I. A. Trujillo-Priego, and B. A. Smith, "How many days are necessary to represent an infant's typical daily leg movement behavior using wearable sensors?" Physical therapy, vol. 99, no. 6, pp. 730–738, 2019.

[24]. S. M. McKay and R. M. Angulo-Barroso, "Longitudinal assessment of leg motor activity and sleep patterns in infants with and without down syndrome," Infant Behavior and Development, vol. 29, no. 2, pp. 153–168, 2006.

[25]. N. Jalloul, "Wearable sensors for the monitoring of movement disorders," Biomedical journal, vol. 41, no. 4, pp. 249–253, 2018.

 ISBN: 978-1-61208-917-1

Field Monitoring of Atmospheric Icing Events - A Case Study

Adeel Yousuf, Pavlo Sokolov & Muhammad S. Virk
Arctic Technology & Icing Research Group
UiT – The Arctic University of Norway
Email: yousuf.adeel@uit.no

***Abstract*— Icing at high altitudes is a major concern for energy sector and infrastructure development. Many icing models exist to predict and analyse icing conditions based on physical or analytical models. This paper presents a field study of meteorological icing events to estimate the Liquid Water Content (LWC) and droplets Median Volume Diameter (MVD), based on ice load from a single cylinder ice collector instead of using multi cylinder ice collector. In this study, ISO 12494 is used to analyse the data from a field ice monitoring station installed in Arctic region of northern Norway. This meteorological station consists of various icing sensors, weather sensor and web camera. Multiple icing events are recorded and analysed with a focus to estimate LWC and MVD using accreted ice mass from single cylinder ice collector. It is noted that accuracy for MVD and LWC estimation can be improved by using smaller time windows of icing events.**

Keywords- Atmospheric icing; Meteorological data; Icing sensor; ISO-12494.

I. INTRODUCTION

Ice accretion poses significant challenges at high latitudes or in cold climatic regions around the world, affecting aviation, construction, and energy sectors. The ice accretion on aircraft can deteriorate its aerodynamic performance. Similarly, ice may accrete on suspension bridge structures that can pose a traffic safety risk resulting in long bridge closures [1]. Blade icing on wind turbines may incur Annual Energy Production loss of 2% – 30%, change the blade aerodynamics, damage onboard controllers and cause safety risk to nearby population due to ice shedding [2] [3]. Similarly, ice accretion on power lines can result in the tower collapse. There're multiple *direct* & *indirect* ways to detect icing on structure. Direct methods normally read on-site sensors or sense changes in different physical quantities (capacitance, vibrations, *etc.*), whereas indirect approaches make use of meteorological parameters such as temperature, dewpoint, *etc.* & apply different data analysis techniques to remotely evaluate ice presence. Extensive literature work is available on both ice detection methodologies [3]-[6]. This paper focuses on the indirect approach using ISO-12494 method for ice detection leading to the calculation of LWC and droplets' MVD. ISO-12494:(2001) formulates a standard for atmospheric ice modelling and field measurements. It suggests using a reference ice collector (0.5 m length, 30 mm diameter) of vertical (freely rotating) cylinder exposed to icing conditions (10 m.a.g.l.).

Better knowledge about ice loads helps to improve the design and safety of structures in icing conditions. Different researchers have used ISO 12494 methodology to estimate ice loads on structures. Hämäläinen *et al.* [7] calculated icing related wind energy production losses by developing Finnish Icing Atlas after combining datasets of NWP and ice-growth model of ISO-12494. Sokolov *et al.* [8] used ISO-12494 to estimate Liquid Water Content (LWC) values in multicylinder assembly for dry ice monitoring to draw comparison of volume weighted averaging & spectrum averaging of droplets. Molkoselkä *et al.* [9] implemented ICEMET cloud droplet and imaging sensor in icing wind tunnel to determine LWC and droplets Median Volume Diameter (MVD) for mixed icing conditions using ISO-12494 standard for single rotating cylinder. Han [10] presented scaling method technique to determine LWC for glaze/rime ice from experimental ice thickness measured using 3D laser scanner. Rydblom *et al.* [11] introduced a cost-effective solution to measure MVD & LWC using Droplet Imaging Instrument (DII) for weather station in Sweden and validated its performance for Supercooled Liquid Droplets (SLD).

This paper used a freely rotating single cylinder to model ice load on structure. For this purpose, a meteorological weather station was designed and installed in northern Norway at Linken Narvik mountain (1006 m.a.s.l.). The area is prone to icing events. The primary aim of using the meteorological and icing data on the reference collector is to employ the ISO 12494 standard to estimate the MVD and LWC values from the measured field meteorological data. The practical usage of the recovered values of MVD and LWC is that they can be used in the subsequent analysis for the purposes of icing load estimations, extreme value analysis and to build a "catalogue" of MVD/LWC values, which can be useful for the Weather Research Forecast (WRF) simulations in the local geographical conditions. While numerical modelling and laboratory experiments (using icing tunnel) are two other techniques to model/measure the extent of icing, field ice monitoring method used in this paper offers high accuracy but at the expense of cost and time.

Section-II of this paper describes the analytical modelling theory for the calculation of MVD & LWC in the light of ISO-12494 standard. Section-III provides a description of installed weather station, followed by the obtained results for field ice monitoring in Section-IV. A brief conclusion is presented in Section-V.

II. ANALYTICAL MODEL

Ice mass accumulation on the man-made onshore objects primarily comes from atmospheric icing, *i.e.*, in-cloud or precipitation icing. For both the in-cloud icing and freezing rain/drizzle, the process of icing originates from the impingement of the supercooled water droplets onto the object in question. The main equation in the analytical modelling of

 ISBN: 978-1-61208-917-1

icing, which describes the rate of icing per unit time is given as (ISO 12494, 2001):

$$\frac{dM}{dt} = \alpha_1\alpha_2\alpha_3 wAv$$

In this equation, otherwise known as "*Makkonen model*" [12], *A* is the cross-sectional area of the object (*with respect to the direction of the particle velocity vector, v; A = LD, where L is the length of the object in z-direction, and D is the characteristic length of the object, i.e., chord length, leading edge diameter, cylinder diameter, etc*.), *w* is the liquid water content, α_1 is the collision efficiency, α_2 is the sticking efficiency, α_3 is the accretion efficiency. The correction factors α_1, α_2 and α_3 represent different processes that may reduce d*M*/d*t* from its maximum value *wAv* [*the units of wAv term in the ISO 12494 standard are g/s (equivalent to the dimensions of dM/dt). The value of dM/dt = vAw is the theoretical maximum impingement rate*]. These correction factors vary between 0 and 1. Factor α_1 represents the efficiency droplets collision, i.e., it is the ratio of the flux density (*in this particular case it is the mass flux (flow) rate*) of the droplets that hit the object, to the maximum flux density, which is a product of the mass concentration of the droplets, *w*, and the velocity, *v*, of the droplets with respect to the object.

While under the ISO 12494 methodology, it is commonly assumed that for the supercooled water droplets, smaller in size than what can be classified as the Supercooled Large Droplets (SLD, with MVD (*d*) > 50 μm), the sticking efficiency α_2 is always equal to 1, meaning all impinging droplets stick on impact, the same may not be true for the accretion efficiency α_3. Consequently, if the value of α_3 is reduced from 1, the ice growth can be classified as "wet", meaning that there is some loss of mass flux due to runback water and water droplets shedding, before they freeze. In this case the glaze ice will be formed. If the value of α_3 is equal to 1, then all impinging droplet freeze on impact. While, in reality, the recorded icing events were a mix of wet and dry ice growth, the fundamental simplification has been made in this study that $\alpha_2 = \alpha_3 = 1$, i.e., all impinging droplets stick and freeze on impact. This is done in order to avoid the uncertainties, pertaining to the calculation of the iced surface thermodynamics, as the available measurement data may be insufficient for this purpose. Furthermore, since the Makkonen model equation described above has two unknowns (α_1 and *w*), and there is only one reference collector installed, the calculation procedure first starts with a "guess" of LWC content. For the purposes of this study the range of *w* is $0.01 < w < 8$ g/m^3. The algorithm first starts with a prescribed LWC and then attempts to find such a MVD value, which produces "optimum" value of α_1 to minimize the error. The algorithm continues to sweep through the rest of LWC values till the "optimum" value is found for both α_1 and *w*, which minimizes the modelling error of measured accreted ice mass *M*. Figure 1 describes flowchart functionality for this method.

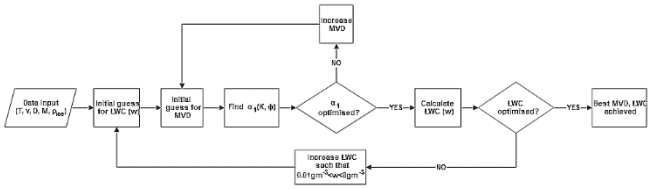

Figure 1. Method used in this study to estimate LWC and MVD

The overall collision efficiency α_1 is evaluated using the ISO 12494 formulae as:

$$E = A - 0.028 - C(B - 0.0454)$$

where constants *A*, *B*, and *C* are defined as:

$$A = 1.066K^{-0.00616}\exp(-1.103K^{-0.688})$$
$$B = 3.641K^{-0.498}\exp(-1.497K^{-0.694})$$
$$C = 0.00637(\phi - 100)^{0.381}$$

K and ϕ are the dimensionless droplet's inertia and Langmuir parameter (sometimes also referred as impingement parameter), respectively and they are given as:

$$K = \frac{2\rho_p r_p^2 u}{9\mu_f C} = \frac{\rho_p d_p^2 u}{18\mu_f C}$$
$$\phi = Re^2/K$$

In which *C* is the characteristic length of the object, in case of cylinder *C* = *R*, where *R* is the cylinder radius. As it can be seen from the equations above, by manipulating the MVD value *d* the necessary change in the values of α_1 is achieved.

III. FIELD ICE MONITORING STATION

The field ice monitoring station used in this study, consists of a Campbell CR1000- data logger, which is interfaced with multiple meteorological sensors: wind speed/direction sensor (Lambrecht EOLOS), IR based ice detection sensor (HoloOptics T44) and ice load sensor (SAAB/Combitech). The ice load sensor consists of a freely rotating, heated single cylinder as per ISO-12494 standard. The setup also includes a web camera which was focused on the ice load sensor for verification of detected icing event. Data is recorded at the online server of Volue Instrument Technology AS via GSM module with a resolution interval of 1 minute for all sensors and 30 min for the web camera. Meteorological observations include average air temperature (°C), wind speed (m/s), wind direction (degrees), icing presence (0/1), ice mass (g), ice mass increment from previous value (g) and relative humidity (%RH). A brief description of these sensors is provided in Table-1. This filed icing station (Figure 2) was installed in Arctic region of northern Norway at Linken Narvik mountain (1006 m.a.s.l.).

Figure 2. The installed weather station at Linken Narvik

TABLE 1. BRIEF DESCRIPTION OF SENSORS USED FOR ICE MONITORING WEATHER STATION IN THIS STUDY

Sensors		Parameter Measured	Specifications
HoloOptics T44		Ice Presence [Ice/No Ice]	Principle of operation: Presence of ice is indicated when 85%-95% of probe surface is covered with 0.01-0.03mm of ice. If <25% of probe surface is covered, icing indication stops
Lambrecht EOLOS		Air Temp RH Wind Speed / Direction	Air temp. resolution: 0.1°C %RH resolution: 0.5% Wind direction resolution: 1° Wind speed resolution: 0.1ms^{-1}
SAAB / Combitech Ice Monitor		Icing Mass	Analogue output (4-20mA); Accuracy: ±50g Resolution = 4g (Max: 10kg) Freely rotating cylinder length = 0.5m Its bearing is electrically heated at constant temp. of 1°C

Data collected from the weather station is sorted and analysed to detect meteorological icing events. Raw data for ice-mass (in kgm^{-1}) as observed by ice load monitor is *smoothed* using local regression with weighted linear least squares and a 2nd degree polynomial model. 15 data-points are taken as a span for calculating the smoothed values while assigning lower weight to outliers. The smoothed ice mass values are treated for calculating LWC & MVD using the ISO-12494. Sticking efficiency (α_2) and freezing efficiency (α_3) are taken as 1 to simulate dry growth measurement of ice. Moreover, the increment of iced cylinder diameter is assumed to follow the following relationship:

$$D = \sqrt{\frac{(4 \times m)}{\pi \rho_{ice}} + D_{uniced}^2}$$

Here, 'm' represents ice-mass after applying *smoothing filter*, 'ρ_{ice}' is the ice density (*the constant value of 700 kgm^{-3} has been chosen for this study as it is deemed to be a "middle-point" between the soft and the hard rime ice types and typical type of ice present in this region*) and 'D_{uniced}' denotes original diameter of cylinder before experiencing icing (equal to 30 mm). Since ISO-12494 method gives better results for high wind speeds, so only those data-points are evaluated where corresponding wind speed > 3ms^{-1}. Similarly, ice shedding events are also neglected.

IV. RESULTS

From the recorded data sets from icing station, icing events are classified as *long-term* if they span more than 3 hours, and *short-term* otherwise. For this purpose, the corresponding calculations for long-term icing events are made on 180 min interval, whereas short-term icing events are taken as whole. For analyzing the trend across different icing events, mean values of LWC, temperature, RH, ice mass are plotted against the icing event number. Visuals obtained from the camera are used to verify the detected icing events.

1) *Icing Events – December 2020*

One short-term & two long-term icing events were identified on 10th Dec 2021. Figure 3 shows the raw data results from all sensors against time (*Central European Summer Time; CEST*) for specified icing events, whereas mean values for these parameters including MVD are plotted. The temperature during the first icing event increased with time from –2.8 °C to –1.4 °C and wind speed varied between 0.6 ms^{-1} – 6 ms^{-1}.

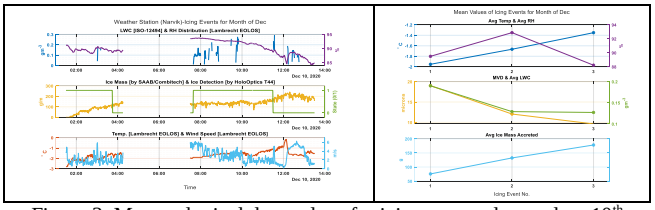

Figure 3. Meteorological data values for icing events detected on 10th December 2020

LWC could only be calculated at few data points during this event, where wind speed was around 5ms^{-1} but greater than 3ms^{-1} & RH > 90%. This is due to the constraint of K < 0.25 being reached for those points. Below this value the ISO 12494 is no longer valid and thus this data is filtered out. During second icing event ice mass rate appears to be slower than first & third events. HoloOptics ice sensor showed ice presence during all icing events but turned off for a portion of time as it can't detect icing thickness less than 0.01mm or when the probe surface is less than 25% covered with ice OR both. Two icing events are separated from each other in Figure 3 as there was a gap of around 3 hours. However, their average values are shown in the same figure to draw comparison among parameters. Timeline images in Figure 4 show the

accreted ice on ice-load monitor depicting a gradual increase in iced cylinder diameter. These images also verified the icing events detected from the meteorological data.

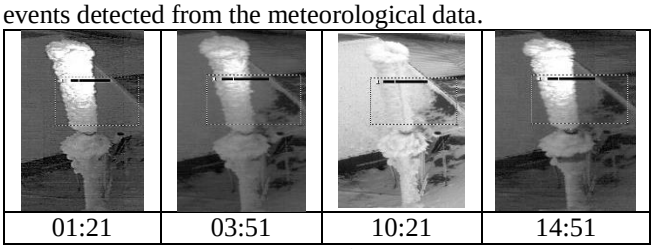

Figure 4. (Dec 10, 2020) Timeline of icing events recorded between 01:21—14:21 hrs. Dull light observed in an image captured on 14:51 is due to polar nights in Narvik during December.

2) Icing Events – January 2021

During the month of January 2021 a long icing event was observed starting from 14th Jan ,18:30hrs – 17th Jan 00:30 hrs. For analysis purpose, this icing event is divided into 18 short icing events, each one with the duration of 180 min (Figure 6: right image). Figure 5 shows the datasets for atmospheric temperature, relative humidity, calculated LWC, *etc.* against time, in addition to mean values of these parameters (including MVD) for corresponding icing event. While considering the ice mass and temperature in Figure 5 which almost continuously increased till the last icing event, high values of LWC are achieved when %RH > 90% and wind speed is around 5 ms^{-1}. It's more evident on 11:15—20:00 (15th Jan). The values of LWC in Figure 5 refer to ISO-12494 equations where it has been conditioned with wind speed in acceptable range (> 3ms^{-1}) and a positive change in ice mass; undefined LWC values against time fail either one or both the conditions. Infrared ice detection sensor remains turned on for whole duration defining it as a long meteorological icing event.

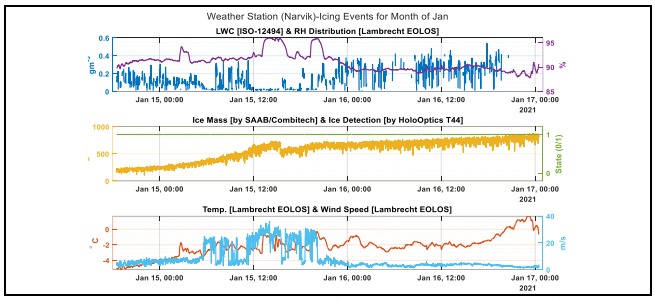

Figure 5. Meteorological data values for icing events detected from 14-17 January, 2021.

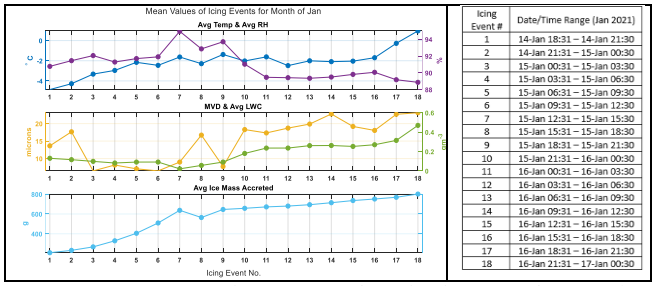

Icing Event #	Date/Time Range (Jan 2021)
1	14-Jan 18:31 – 14-Jan 21:30
2	14-Jan 21:31 – 15-Jan 00:30
3	15-Jan 00:31 – 15-Jan 03:30
4	15-Jan 03:31 – 15-Jan 06:30
5	15-Jan 06:31 – 15-Jan 09:30
6	15-Jan 09:31 – 15-Jan 12:30
7	15-Jan 12:31 – 15-Jan 15:30
8	15-Jan 15:31 – 15-Jan 18:30
9	15-Jan 18:31 – 15-Jan 21:30
10	15-Jan 21:31 – 16-Jan 00:30
11	16-Jan 00:31 – 16-Jan 03:30
12	16-Jan 03:31 – 16-Jan 06:30
13	16-Jan 06:31 – 16-Jan 09:30
14	16-Jan 09:31 – 16-Jan 12:30
15	16-Jan 12:31 – 16-Jan 15:30
16	16-Jan 15:31 – 16-Jan 18:30
17	16-Jan 18:31 – 16-Jan 21:30
18	16-Jan 21:31 – 17-Jan 00:30

Figure 6. (Jan 14-17)-[Left]: Mean temp/RH, droplets' MVD/ LWC & ice mass accreted on ice load monitor against different icing events. [Right]: Exact time divisions for icing events.

Examining the timeline images in Figure 7 shows rime ice appearance. A significant outer diameter change is observed for ice load monitor which allows to capture more striking droplets alongside an increase in %RH. Meanwhile taking ice-mass graph (in Figures 5, 6) into consideration, ice mass curve depicts a nonlinear increase for ice mass accumulation till 12:30 on 15th Jan after which the curve follows a linear fashion up till 17th Jan. %RH stayed above 90% for most of the time. Rest of the images show rime ice that apparently got hardened due to high wind speed and negative temperature on 15th Jan, possibly freezing the available captured water content.

Figure 7. Timeline of icing events recorded between Jan 14—Jan 16. The starting image on Jan 14 shows little icicles present on cylinder surface.

3) Icing Events – February 2021

A long-term meteorological icing event spanning about 18hrs is detected on 7th Feb. The event is subdivided into six small icing events, each one of 180min duration. Figure 8 shows the plots of different meteorological parameters based on data collected from sensors. Temperature change of approx. 1.5°C is observed during daytime which then again decreased till night. Relative humidity stayed close to 90% most of the time however high wind speed is observed ranging from 1.6 ms^{-1} – 12.8 ms^{-1}. Cylinder endures a slight increase in diameter as rime accretes, as can be seen in timeline images in Figure 9.

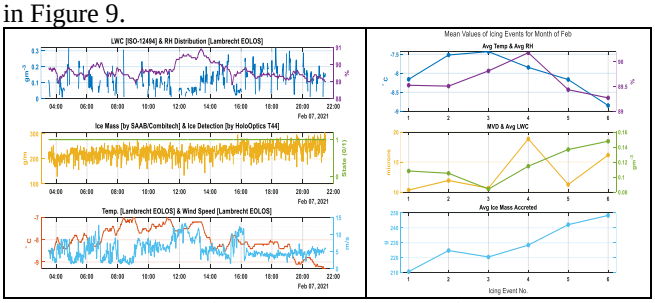

Figure 8. (Feb 7)-[Left]: Icing station data values for %RH/LWC, ice-mass/ice detection & temp./wind speed. [Right]: Mean temp/RH, droplets' MVD/mean LWC & ice mass accreted on Combitech ice-monitor against different icing events.

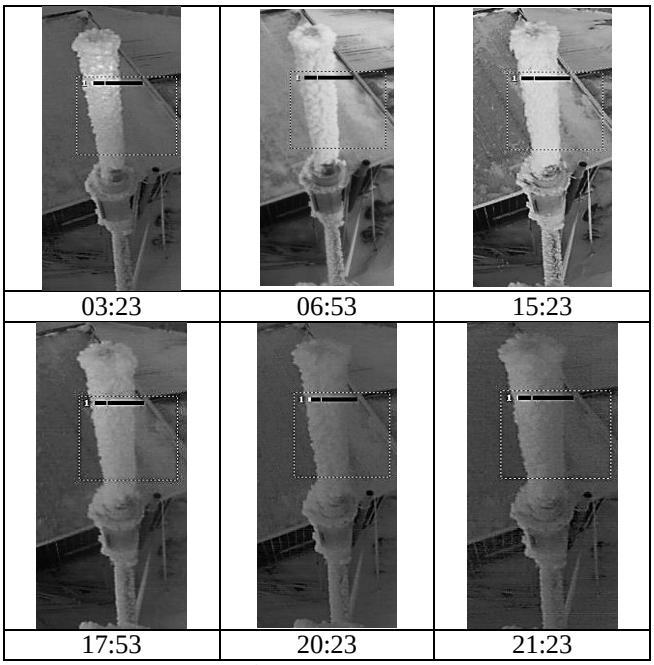

Figure 9. (Feb 7) Timeline of icing events recorded between 03:23—21:23

B. *Effect of Data Resolution*

Figure 3 showed ice accretion results on 10th Dec with 180min timespan for events 2 & 3. To assess how MVD accuracy changes with resolution of time window, same icing events (07:31-13:30) are subdivided into smaller 90min icing events. Figure 10 presents the comparison of mean values of temp., %RH, LWC, *etc.*

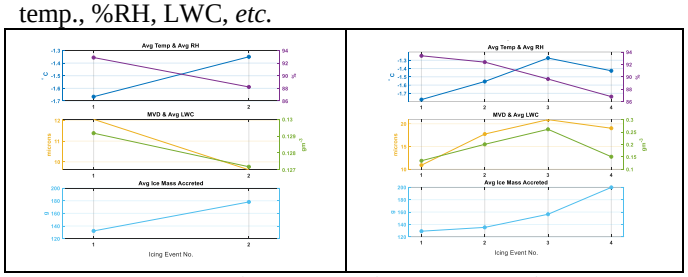

Figure 10. Comparison of mean values of icing parameters for a total icing duration of 6hrs (07:31-13:30) on 10th Dec. Left image displays results when icing duration is split into 2 icing events (comprised of 180min duration each), whereas right side image displays results when same duration is split into 4 small icing events (90min duration each).

It can be observed that improved results can be obtained with high resolution (i.e., splitting into smaller duration of icing events). MVD values have changed from (12, 9.6) µm to (10.8, 17.7, 20.9, 19) µm; similar is the case with other parameters. Increasing the resolution for icing event means studying fewer no. of droplets impinging the cylinder surface in a stipulated time, which removes potential outliers in data and gives better results but at the expense of more computation time.

V. Conclusion And Future Work

The paper presented an analytical method for ice modelling technique using field icing events data where a single cylinder assembly is used to estimate MVD and LWC. The method used in the study implemented ISO-12494 standard cylinder (0.5m in height, 30mm diameter) by Combitech as an ice load monitor. Analysis show that LWC and MVD can also be estimated using single cylinder ice collector instead of just using the multicylinder ice collector assembly. Multiple icing events were recorded and analysed. During analysis longer icing events spanning several hours of continuous ice accretion are subdivided into smaller events (3hrs). It was noted that accuracy for MVD and LWC can be improved by using smaller time intervals instead of longer intervals of icing events. As a future work the results can be further furnished to compare the accuracy using multi-cylinder network and assist the study of thermodynamics and heating phenomena in order to develop anti/deicing system. Due to high accuracy of field icing results, they can also be used to develop catalogues for Weather Research & Forecasting (WRF) simulations. Such measurements will provide a foundation for risk assessment during infrastructure development in Arctic region exhibiting similar climatic conditions.

Acknowledgment

The work reported in this paper is supported by the CoARICE project funded by Norwegian Research Council & NABL project funded by EU Kolarctic CBC.

References

[1] K. Kleissl and C. T. Georgakis, "Bridge ice accretion and de- and anti-icing systems: A review," in *The 7th International Cable Supported Bridge Operators Conference*, 2010. pp. 161-167

[2] S. Barber, Y. Wang, S. Jafari, N. Chokani, and R. S. Abhari, "The Impact of Ice Formation on Wind Turbine Performance and Aerodynamics," *Journal of Solar Energy Engineering*, vol. 133, no. 1, February 2011.

[3] K. Wei, Y. Yang, H. Zuo, and D. Zhong, "A review on ice detection technology and ice elimination technology for wind turbine," *Wind Energy*, pp. 433-457, 29 December 2019.

[4] U. N. Mughal and M. S. Virk, "Atmospheric Icing Sensors – An Insight," in *SENSORCOMM 2013: The Seventh International Conference on Sensor Technologies and Applications*, Barcelona, 2013. pp. 191-199

[5] U. N. Mughal, M. S. Virk, and M. Y. Mustafa, "State of the Art Review of Atmospheric Icing Sensors," *Sensors and Transducers*, vol. 198, no. 3, pp. 2-15, 31 March 2016.

[6] M. S. Virk, U. N. Mughal and G. Polanco, "Atmospheric Ice Accretion on Non-Rotating Vertical Circular Cylinder," *World Journal of Engineering and Technology*, vol. 3, no. 3, pp. 284-289, 2015.

[7] K. Hämäläinen and S. Niemelä, "Production of a Numerical Icing Atlas for Finland," *Wind Energy*, vol. 20, no. 1, pp. 171-189, 2016.

[8] P. Sokolov and M. S. Virk, "Modeling of Dry Ice Accretion on Cylinders – A Case Study of Present Analytical State," in *International Workshop on Atmospheric Icing of Structures (IWAIS)*, Reykjavik, 2019.

[9] E. Molkoselkä, V. Kaikkonen and A. Mäkynen, "Instrument and Method for Measuring Ice Accretion in Mixed-Phase

Cloud Conditions," in *IEEE Instrumentation and Measurement Technology Conference (I2MTC)*, Dubrovnik, 2020. pp. 1-5.

[10] Y. Han, "Theoretical and Experimental Study of Scaling Methods for Rotor Blade Ice Accretion Testing," The Pennsylvania State University, 2011.

[11] S. Rydblom, B. Thörnberg and E. Olsson, "Field Study of LWC and MVD Using the Droplet Imaging Instrument," *IEEE Transactions on Instrumentation and Measurement*, vol. 68, no. 2, pp. 614-622, February 2019.

[12] L. Makkonen, "Models for the growth of rime, glaze, icicles and wet snow on structures," *Philosophical Transactions of the Royal Society A: Mathematical, Physical and Engineering Sciences*, vol. 358, no. 1776, pp. 2913-2939, 2000.

 ISBN: 978-1-61208-917-1

Wave Height Estimation Using a Novel Seaweed-Attached Sensor

Masoud Emam, Caroline Press, Hamed Jafarzadeh,
Marco Belcastro, Brendan O'Flynn
Tyndall National Institute
University College Cork (UCC)
Cork, Ireland
Email: [masoud.emam, caroline.peres, hamed.jafarzadeh,
marco.belcastro, brendan.oflynn]@tyndall.ie

Joanne Casserly, Frank Kane
Marine Institute
Rinville, Oranmore
Galway, Ireland.
Email: [joanne.casserly, frank.kane]@marine.ie

***Abstract*— The growth rate of seaweed is significantly affected by wave parameters and sea conditions. The wave characteristics in an aquaculture farm is normally measured using expensive equipment, which is not affordable for many farmers or researchers, and is not easily relocated from place to place to evaluate wave conditions in a variety of locations. In this paper, a sensor fusion method is presented which can estimate wave height using the data logged by a multi modal low-cost seaweed-attached sensor system. The sensor was developed for use in an Aquaculture scenario. This method is based on combination of extended Kalman filter and artificial neural networks. Regarding the importance of studying the impact of wave on seaweeds growth rate, this method will avail many researchers to use wave height data in their study to fill the gap in knowledge of the impact of water motion on aquaculture and maximising of seaweed harvests.**

Keywords; Seaweed attached sensor; Aquaculture; Underwater sensor; Embedded system; Kalman filter; Artificial Neural Network.

I. INTRODUCTION

According to the "*fishery and aquaculture statistics*" published by the Food and Agriculture Organisation (FAO) [1], the contribution from aquaculture to total fish production reached 46.0% in 2018 as compared to 25.7% in 2000. This rapid growth in fish farming activities causes environmental sustainability concerns [2]. As production increases, so two the demand on the environment to provide more nutrients and the waste generated increases. Another impact on economic sustainability comes from the increased maintenance and labour costs associated with increased production.

One promising solution to sustainable aquaculture is to employ the practice of Integrated Multi-trophic Aquaculture (IMTA) . IMTA is an aquaculture farming method where the by-products and wastes of one aquatic species, for example fish, is utilised as food for another species, such as seaweed or shellfish. New approaches, such as those developed in the IMPAQT project [3], aim to integrate the IMTA model, smart systems, and sensors for monitoring, data modelling and intelligent management systems [4].

Seaweed growth rates are considerably affected by water motion and flow rate. In low level water motion, seaweeds absorb less nutrients and CO2, which is limiting the growth. High movement rates, on the other hand, can dislodge kelps and reduced productivity as a result of forcing them to develop larger holdfasts [5]. According to Hurd [6], to understand how water motion can affect the growth rate of seaweeds, the influence of other environmental factors should be measured and accounted for in aquaculture site management and operation.

Several studies have investigated this topic, such as [7], [8], and [9], where water motion rates and wave exposure were not directly measured with wave sensors/loggers, such as Acoustic Doppler Current Profilers (ADCP), wave buoys, but were indirectly measured using wind speed and incidence, and distance to coastline to estimate the wave exposure index [10]. Using this method it was possible to categorise large geographical locations as "high exposure" or "low exposure". According to Lindegarth and Gamfeldt [11], using this categorical variable method instead of a continuous-type variable results in very different explanations of the importance of environmental factors. Furthermore, Focht and Shima [12], found that the correspondence between in-situ measurements by accelerometers and a wave-rider buoy and a priori assessments of wave exposure is limited.

Various research, such as [12]-[14], presented solutions to the problem of measuring water motion using inexpensive sensors developed using commonly available materials. Lyman et al. [14], developed a low-cost open-source pressure transducer to record wave height using a PVC pipe as housing. In [12], fine-scale wave exposure in different locations have been measured using accelerometers, and compared with a nearby deployed wave-rider buoy. Their analysis shows that there was a significant fine-scale variation in the wave movement, as a result of changes in acceleration, timing, and frequency of wave events.

Evans and Abdo in [13], designed a structure that is attached to a HOBO Pendant G acceleration data logger, moored to the seafloor, and deployed adjacent to a wave-rider buoy. They showed that the wave motion data logged by the accelerometer is correlated with the daily average, maximum Wave-Rider Buoy (WRB), tidal data and found it to be highly correlated with daily average total wave height. The authors discussed that using a faster sampling rate for accelerometer (with increased data storage), more detailed water movement parameters, such as velocities, forces, and wave period; could be measured and determined. It would also enable a more detailed analysis of the data using spectral analysis. They

 ISBN: 978-1-61208-917-1

conclude that, their method allows researchers to collect additional water movement data where advanced devices are not available or too costly.

In another study by Mullarney and Pilditch [15], the HOBO Pendant G Accelerometers is attached to the kelp stipe by tying it at fixed intervals up the stipe bundle. Pressure and velocities were measured by an Acoustic Doppler Current Profilers (ADCP) for this study. The objective of the research was to find the response of kelp to the wave movement.

According to the review of literature that has been presented, measurements of wave height and/or water motion is critical in aquaculture and has been studied in many research publications. However, all the solutions and research discussed above have problems in common, such as the typically large size of the sensors systems that limits the deployment method; power requirements such as cables, external power supplies, and data recovery. On the other hand, a low-cost miniature wave measurement solution has been presented in [16] and [17]. To aid in in-situ monitoring for IMTA aquaculture farm sites, a seaweed monitoring device was developed, which is described in detail in [18].

In this paper, a method based on sensor fusion and Artificial Intelligence (AI) is proposed in order to estimate current and wave using data recorded by the attached seaweed sensor presented in [18]. This method can avail many researchers to use wave height data in their study and fill the gap in knowledge of exact impact of water motion on aquaculture. To achieve this method, the seaweed-attached sensors have been deployed in an IMTA site and the correlation between the data recorded by the sensor and wave height have been studied. The results showed a strong correlation and the next step is to train a neural network to estimate wave height using data logged by seaweed-attached sensor.

The remainder of the paper is organised as the following. In Section II, the methodology of suggested method is presented and feasibility of the method is investigated in Section III where the initial result from a deployment is studied. At the end, in Section IV, the paper is concluded.

II. METHODOLOGY

The seaweed attached sensor, AquaBit (see Figure 1.), has been originally designed to measure ambient parameters relevant to seaweeds, such as light, temperature, depth, and motion [18]. However, this sensor has significant potential to be used in indirect measurement of other parameters based on fusion of the readings from different sensors embedded in AquaBit. In this section, a method is proposed to estimate current strength and wave height.

The embedded IMU sensor consists of a 3-axis accelerometer and a 3-axis gyroscope. The accelerations and angular velocities are sampled with the frequency of 12.5 Hz and recorded in the internal flash memory of AquaBit. This sampling frequency provide much higher accuracy in comparison with a data buoy which normally operate with a very long sampling interval in range of minutes.

Motion and displacement of the seaweed-attached sensor is the result of current and wave. Faster motion is the result of stronger wave or current [19]. Therefore, if we can calculate the motion of the attached sensor, we can estimate the strength of current or wave. Theoretically, acceleration is the second time-derivative of position, and vice versa, position is the second integral of acceleration. Therefore, we should be able to calculate the position of AquaBit easily from the accelerations measured by the IMU. However, this calculation results in huge position error as the consequence of measurement noise.

Figure 1. Seaweed attached sensor, AquaBit Unit

On the other hand, it is very hard to find the exact function that maps the motion of attached sensor to wave or current. The main reason is that the AquaBit is attached to seaweed blades and to establish the function, the exact hydro dynamic model of seaweed blades and AquaBit are needed which is hard (or even impossible) to find in the context of the fast growth of seaweeds.

The proposed method of this paper is to use an Extended Kalman Filter (EKF) and Artificial Neural Network (ANN) to estimate current and wave base on the readings from IMU sensor. The EKF is employed to cope with the noise in measurement and the ANN is trained in such a way that maps the accelerations to current and wave states.

The EKF is a well-known optimal state observer for nonlinear systems, which can estimate the state of system using noisy measurements of system output [20]. EKF has also been widely employed as a sensor fusion method to estimate the orientation of an object using angular velocities and linear acceleration experienced by the object, [21][22].

The proposed method is to feed IMU measurements to an EKF to estimate the orientation of the IMU with respect to an Earth-Fixed coordination Frame (EFF). The EEF is a three-dimension orthogonal coordination frame fixed to the earth. The X-axis is aligned with the North direction in the opposite direction of gravity, Y-axis is aligned with the West direction, and Z-axis is the cross product of X and Y, which is in the opposite direction of gravity. Using the orientation of the IMU w.r.t. EFF, we will be able to reject the effect of gravity on measurements of accelerometer and estimate the accelerations in EFF.

Artificial intelligence, or more specifically Artificial Neural Networks (ANN), is a good solution when it is difficult to directly measure a physical parameter but some other related parameters are more accessible and easy to measure. For example, in the case of the scenario described in this paper, it is impossible to measure wave height on each

seaweed growth line in an aquaculture farm. However, it is possible to measure the acceleration and angular velocity experienced by seaweeds using AquaBit. Therefore, we can train an ANN to estimate wave height from AquaBit measurements.

To train the ANN, AquaBit units will be deployed as close as possible to a current meter or wave logger/sensor. Then, using the IMU measurement of AquaBit, as inputs, and the data logged by current meter/wave sensor, as outputs, are joined to shape a dataset. This dataset is used to train and test the ANN. Then, this ANN is used to map acceleration to current or wave.

III. PILOT RESULTS

To test the feasibility of the proposed method, data collected in one of the AquaBit deployment in the Marine Institute aquaculture research site (Lehanagh Pool), Galway, Ireland is used. In this deployment, AquaBit units have been attached to artificial seaweeds, as shown in Figure 2.

Figure 2. An AquaBit unit attached to artificial seaweed.

The data recorded by the IMU sensor of AquaBit in this deployment have been compared with tilt data recorded by the data buoy of the same site.

To evaluate the feasibility of the proposed method the correlation between magnitude of tilt data and the magnitude of reading from AquaBit gyroscope in frequency domain is studied using Pearson correlation coefficient.

The tilt data are recorded as the maximum and minimum value of tilt experienced around X- and Y-axis (EEF) during a 10 minute period. The magnitude of tilt is calculated as in (1) and (2).

$$Tilt_{max} = \sqrt{Tilt\_X_{max}^2 + Tilt\_Y_{max}^2} \quad (1)$$

$$Tilt_{min} = \sqrt{Tilt\_X_{min}^2 + Tilt\_Y_{min}^2} \quad (2)$$

On the other hand, the magnitude of readings from gyroscope is calculated as in (3) and (4).

$$W_{max} = \sqrt{w\_x_{max}^2 + w\_y_{max}^2 + w\_z_{max}^2} \quad (3)$$

$$W_{min} = \sqrt{w\_x_{min}^2 + w\_y_{min}^2 + w\_z_{min}^2} \quad (4)$$

where, w_x_{max}, w_y_{max}, and w_z_{max} are the maximum angular velocity around X-, Y-, and Z-axis (sensor coordination frame) during a 10 minute period. Note that, the time period for maximum/minimum calculation is exactly the same for data buoy and AquaBit.

Since these measurements are compared in frequency domain, the Fast Fourier Transformation (FFT) is used to transform tilt and angular velocities into frequency domain.

The Pearson correlation coefficient for the FFT of $Tilt_{max}$ and the FFT of W_{max} is 0.84 with p-value of 5×10^{-97}; and for the FFT of $Tilt_{min}$ and the FFT of W_{min} is 0.85 with p-value of 1×10^{-99}, which means the variation in tilt can be calculated using angular velocities by a linear function. The tilt values from the data buoy approximately represents wave height – the higher the wave height the more tilt measured by the buoy measures. As the tilt measured by the buoy is correlated with the angular velocity measured by the sensor device, we conclude that the wave height could be estimated by the angular velocity. This supports the expectation that a sensor fusion algorithm for accelerometer and gyroscope could provide good estimates of wave height and energy.

IV. CONCLUSIONS AND FUTURE WORK

In this paper, we presented a work in progress, a novel method of estimation of wave height for cost effective research project. The method translates the data collected by a 6 Degree of Freedom (DoF) IMU (accelerometer and gyroscope) into wave height by combining EKF and ANN. The data analysis of a pilot trial showed that the angular velocity is strongly correlated to tilt values recorded by a wave-rider buoy. In other words, wave height or other wave statistical parameters could be estimated using readings from the embedded IMU of AquaBit. The next step is to figure out an ANN and train it to estimate the wave height using the data recorded by the embedded IMU of AquaBit. The hypothesis will continue to be investigated in Flume Tanks [23] (dedicated infrastructure for wave measurements) and the algorithms developed to establish wave height from IMU readings attached to seaweed lines in aquaculture oriented deployments.

ACKNOWLEDGMENT

This work has been funded as part of the IMPAQT project [24] – and it has received funding from the European Union's Horizon 2020 research and innovation programme under Grant Agreement No 774109. Aspects of this publication have been funded in part by a research grant from Science Foundation Ireland (SFI) - co-funded under the European Regional Development Fund under Grant Number 16/RC/3835 – VISTAMILK 16/RC/3835, INSIGHT 13/RC/2077_P2 and CONNECT 13/RC/2077.

 ISBN: 978-1-61208-917-1

REFERENCES

[1] F. Yearbook, "Fishery and aquaculture statistics 2016," *Rome: FAO*, 2019.

[2] M. Føre *et al.*, "Precision fish farming: a new framework to improve production in aquaculture," *biosystems engineering*, vol. 173, pp. 176-193, 2018.

[3] "IMPAQT Project." https://impaqtproject.eu/about-impaqt/ (accessed Sep. 17, 2021).

[4] I. A. Iglesias. "Can integrated multi-trophic aquaculture (IMTA) make an IMPAQT in Europe?" https://thefishsite.com/articles/can-integrated-multi-trophic-aquaculture-imta-make-an-impaqt-in-europe (accessed Sep. 17, 2021).

[5] P. D. Kerrison, M. S. Stanley, M. D. Edwards, K. D. Black, and A. D. Hughes, "The cultivation of European kelp for bioenergy: site and species selection," *Biomass and bioenergy*, vol. 80, pp. 229-242, 2015.

[6] C. L. Hurd, "Water motion, marine macroalgal physiology, and production," *Journal of Phycology*, vol. 36, no. 3, pp. 453-472, 2000.

[7] W. Visch, G. M. Nylund, and H. Pavia, "Growth and biofouling in kelp aquaculture (Saccharina latissima): the effect of location and wave exposure," *Journal of Applied Phycology*, vol. 32, no. 5, pp. 3199-3209, 2020.

[8] L. Kregting, A. J. Blight, B. Elsäßer, and G. Savidge, "The influence of water motion on the growth rate of the kelp Laminaria digitata," *Journal of experimental marine biology and ecology*, vol. 478, pp. 86-95, 2016.

[9] T. Bekkby, E. Rinde, H. Gundersen, K. M. Norderhaug, J. K. Gitmark, and H. Christie, "Length, strength and water flow: relative importance of wave and current exposure on morphology in kelp Laminaria hyperborea," *Marine Ecology Progress Series*, vol. 506, pp. 61-70, 2014.

[10] M. T. Burrows, R. Harvey, and L. Robb, "Wave exposure indices from digital coastlines and the prediction of rocky shore community structure," *Marine Ecology Progress Series*, vol. 353, pp. 1-12, 2008.

[11] M. Lindegarth and L. Gamfeldt, "Comparing categorical and continuous ecological analyses: effects of "wave exposure" on rocky shores," *Ecology*, vol. 86, no. 5, pp. 1346-1357, 2005.

[12] R. C. Focht and J. S. Shima, "Acceleration loggers reveal fine-scale heterogeneity in wave exposure along an open coast," *Estuarine, Coastal and Shelf Science*, vol. 233, p. 106507, 2020.

[13] S. Evans and D. Abdo, "A cost-effective technique for measuring relative water movement for studies of benthic organisms," *Marine and Freshwater Research*, vol. 61, no. 11, pp. 1327-1335, 2010.

[14] T. P. Lyman, K. Elsmore, B. Gaylord, J. E. Byrnes, and L. P. Miller, "Open Wave Height Logger: An open source pressure sensor data logger for wave measurement," *Limnology and Oceanography: Methods*, vol. 18, no. 7, pp. 335-345, 2020.

[15] J. C. Mullarney and C. A. Pilditch, "The differential response of kelp to swell and infragravity wave motion," *Limnology and Oceanography*, vol. 62, no. 6, pp. 2524-2537, 2017.

[16] D. Kennedy, M. Walsh, and B. O'Flynn, "Development of a miniature, low-cost wave measurement solution," in *2014 Oceans-St. John's*, 2014: IEEE, pp. 1-6.

[17] D. Kennedy, M. Walsh, and B. O'Flynn, "Low-cost inertial measurement of ocean waves," in *2014 IEEE Sensor Systems for a Changing Ocean (SSCO)*. 2014: IEEE, pp. 1-2.

[18] C. Peres, M. Emam, H. Jafarzadeh, M. Belcastro, and B. O'Flynn, "Development of a Low-Power Underwater NFC-Enabled Sensor Device for Seaweed Monitoring," *Sensors*, vol. 21, no. 14, p. 4649, 2021.

[19] M. Denny and B. Gaylord, "The mechanics of wave-swept algae," *Journal of Experimental Biology*, vol. 205, no. 10, pp. 1355-1362, 2002.

[20] Q. Li, R. Li, K. Ji, and W. Dai, "Kalman filter and its application," in *2015 8th International Conference on Intelligent Networks and Intelligent Systems (ICINIS)*, 2015: IEEE, pp. 74-77.

[21] J. L. Marins, X. Yun, E. R. Bachmann, R. B. McGhee, and M. J. Zyda, "An extended Kalman filter for quaternion-based orientation estimation using MARG sensors," in *Proceedings 2001 IEEE/RSJ International Conference on Intelligent Robots and Systems. Expanding the Societal Role of Robotics in the the Next Millennium (Cat. No. 01CH37180)*, 2001, vol. 4: IEEE, pp. 2003-2011.

[22] A. M. Sabatini, "Quaternion-based extended Kalman filter for determining orientation by inertial and magnetic sensing," *IEEE transactions on Biomedical Engineering*, vol. 53, no. 7, pp. 1346-1356, 2006.

[23] "LiR National Ocean Facility " http://www.lir-notf.com/ (accessed 2021).

[24] "IMPAQT project." https://impaqtproject.eu/ (accessed 2021).

 ISBN: 978-1-61208-917-1

Tensor-Based Recursive Least-Squares Algorithm with Low Computational Complexity

Ionuţ-Dorinel Fîciu, Cristian-Lucian Stanciu, Laura-Maria Dogariu, Camelia Elisei-Iliescu, and Constantin Paleologu
Department of Telecommunications, University Politehnica of Bucharest, Romania
Email: ionut_dorinel.ficiu@upb.ro, {cristian, ldogariu, pale}@comm.pub.ro, camelia.elisei@romatsa.ro

***Abstract*—Many system identification problems can be addressed based on tensor decomposition methods. In this framework, the conventional Recursive Least-Squares (RLS) algorithm requires a prohibitive amount of arithmetic resources and is sometimes prone to numerical stability issues. This paper presents a low-complexity RLS-based algorithm for multiple-input/single-output system identification, which results as a combination between the exponentially weighted RLS algorithm and the Dichotomous Coordinate Descent (DCD) iterations.**

Index Terms*—*adaptive filter; multilinear forms; recursive least-squares (RLS); dichotomous coordinate descent (DCD); tensor decomposition

I. Introduction

The identification of multilinear forms (or linearly separable systems) can be efficiently exploited in the framework of different applications [1]. Such scenarios can appear in the framework of multichannel systems, e.g., with a large number of sensors and actuators. In these contexts, the basic approach relies on tensor decomposition and modeling techniques, since the multilinear forms can be modeled as rank-1 tensors. The main idea is to combine (i.e., "tensorize") the solutions of low-dimension problems, in order to efficiently solve a multidimensional system identification problem, which is usually characterized by a large parameter space.

For the system identification implementations, which can be decomposed using Multiple-Input/Single-Output (MISO) setups, several tensor-based models were recently proposed [1]. One such decomposition uses the Recursive Least-Squares (RLS) method based on Woodburry's identity to split the unknown system determination into multiple smaller adaptive systems. Despite the fact that the overall complexity is reduced, the algorithm previously introduced as tensor-based RLS (RLS-T) is still dependent on the square of each filter's length, and it is also prone to inherit the problems of classical least-squares solutions [2].

The combination with the Dichotomous Coordinate Descent (DCD) iterations has been established as a possible stable alternative with lower complexity traits, proportional to the filter's length [3]. Based on this idea, the current paper presents a tensorial decomposition for multilinear forms based on the RLS-DCD method. For the identification of an unknown MISO system based on its tensorial form, multiple RLS-DCD shorter filters are employed, which inherit the performance of the classical RLS versions and require lower arithmetic efforts.

In the following, Section II introduces the framework of multilinear forms, while Section III presents the proposed algorithm. Finally, several conclusions are summarized in Section IV.

II. Multilinear Forms

In the framework of a real-valued MISO system, the output signal (at discrete-time index n) is defined as

$$y(n) = \sum_{l_1=1}^{L_1} \sum_{l_2=1}^{L_2} \cdots \sum_{l_N=1}^{L_N} x_{l_1 l_2 \ldots l_N}(n) h_{1,l_1} h_{2,l_2} \cdots h_{N,l_N},$$

where $\mathbf{h}_i = [h_{i,1} \; h_{i,2} \; \cdots \; h_{i,L_i}]^T$ are N individual channels, each one of length $L_i, \; i = 1, 2, \ldots, N$, and the superscript ^{T} denotes the transpose operator. The input signals can be described in the tensorial form $\boldsymbol{\mathcal{X}}(n) \in \mathbb{R}^{L_1 \times L_2 \times \cdots \times L_N}$, having the elements $(\boldsymbol{\mathcal{X}})_{l_1 l_2 \ldots l_N}(n) = x_{l_1 l_2 \ldots l_N}(n)$. Thus, the output signal becomes

$$y(n) = \boldsymbol{\mathcal{X}}(n) \times_1 \mathbf{h}_1^T \times_2 \mathbf{h}_2^T \times_3 \cdots \times_N \mathbf{h}_N^T, \tag{1}$$

where $\times_i, \; i = 1, 2, \ldots, N$ denotes the mode-i product. As we can notice, $y(n)$ is a multilinear form, since it is a linear function of each $\mathbf{h}_i, \; i = 1, 2, \ldots, N$, when the other $N - 1$ components are fixed.

Let us consider the rank-1 tensor $\boldsymbol{\mathcal{H}} \in \mathbb{R}^{L_1 \times L_2 \times \cdots \times L_N}$, with the elements $(\boldsymbol{\mathcal{H}})_{l_1, l_2, \ldots, l_N} = h_{1,l_1} h_{2,l_2} \cdots h_{N,l_N}$, such that $\boldsymbol{\mathcal{H}} = \mathbf{h}_1 \circ \mathbf{h}_2 \circ \cdots \circ \mathbf{h}_N$, where $\circ$ denotes the outer product. In addition, we have $\text{vec}\,(\boldsymbol{\mathcal{H}}) = \mathbf{h}_N \otimes \mathbf{h}_{N-1} \otimes \cdots \otimes \mathbf{h}_1$, where $\text{vec}(\cdot)$ is the vectorization operation and $\otimes$ denotes the Kronecker product. Hence, we can rewrite (1) as $y(n) = \text{vec}^T\,(\boldsymbol{\mathcal{H}})\,\text{vec}\,[\boldsymbol{\mathcal{X}}(n)]$.

Furthermore, we can denote $\mathbf{x}(n) = \text{vec}\,[\boldsymbol{\mathcal{X}}(n)]$ and $\mathbf{g} = \text{vec}\,(\boldsymbol{\mathcal{H}})$. Here, $\mathbf{x}(n)$ is the input vector of length $L_1 L_2 \cdots L_N$ and $\mathbf{g}$ plays the role of a global impulse response (of the same length). Therefore, (1) finally becomes $y(n) = \mathbf{g}^T \mathbf{x}(n)$, while the reference signal results as

$$d(n) = \mathbf{g}^T \mathbf{x}(n) + w(n), \tag{2}$$

where $w(n)$ is the measurement noise, which is uncorrelated with the input signals. The main goal is the identification of the global system $\mathbf{g}$. Equivalently, the identification problem can be formulated in terms of recursively estimating the individual components $\mathbf{h}_i, \; i = 1, 2, \ldots, N$.

 ISBN: 978-1-61208-917-1

III. RLS-Based Algorithms

The faster convergence rate is one of the main advantages of the RLS methods, with respect to the performances obtained by other families of algorithms. However, this convergence aspect comes together with a very high computational complexity. It was previously demonstrated that tensor-based algorithms could produce better results than the classical RLS approach, by splitting the long filter associated with the unknown system identification problem into multiple smaller filters, i.e., into multiple smaller system identification processes. This results in a significant decrease in the number of mathematical operations and improved convergence rates.

Let us consider the estimated impulse responses of the channels, $\widehat{\mathbf{h}}_i(n),\ i = 1, 2, \ldots, N$, and the estimated output, $\widehat{y}(n)$, such that the error signal results in N equivalent ways:

$$e(n) = d(n) - \widehat{y}(n) = d(n) - \widehat{\mathbf{h}}_i^T(n-1)\mathbf{x}_{\widehat{\mathbf{h}}_i}(n), \quad (3)$$

for $i = 1, 2, \ldots, N$, where

$$\mathbf{x}_{\widehat{\mathbf{h}}_i}(n) = \Big[\widehat{\mathbf{h}}_N(n-1) \otimes \widehat{\mathbf{h}}_{N-1}(n-1) \otimes \cdots \otimes \widehat{\mathbf{h}}_{i+1}(n-1) \otimes \mathbf{I}_{L_i} \otimes \widehat{\mathbf{h}}_{i-1}(n-1) \otimes \cdots \otimes \widehat{\mathbf{h}}_2(n-1) \otimes \widehat{\mathbf{h}}_1(n-1)\Big]^T \mathbf{x}(n),$$

with $\mathbf{I}_{L_i}$ denoting the identity matrices of sizes $L_i \times L_i$.

At this point, we can apply the least-squares (LS) error criterion [2] in the context of (2) and (3). Thus, the cost functions can be formulated in N alternative ways, following the optimization procedure of the individual impulse responses. Furthermore, the minimization of these cost functions with respect to $\widehat{\mathbf{h}}_i(n),\ i = 1, 2, \ldots, N$ leads to the set of normal equations, which result in the updates of the individual filters of the RLS-T algorithm [1].

In this idea paper, we propose to use the combination between the DCD iterations and the RLS method, in the tensorial framework. The RLS-DCD algorithm [3] was employed in the past due to its low complexity arithmetic workloads and improved numerical stability. The advantages obtained by using the generalized tensorial model applied with low-complexity RLS algorithms can lead to high convergence/tracking speeds and acceptable computational requirements, an overall design that is suitable for efficient hardware applications.

The proposed tensor-based RLS-DCD (RLS-DCD-T) algorithm is summarized in Table I. For each of the corresponding channels, the RLS-DCD-T is designed with an overall complexity proportional to the length of the associated adaptive filter, in terms of additions and multiplications. No divisions are needed to perform the filter update process or to generate the output information. Consequently, the complexity of the Exponential Weighted RLS-DCD-T algorithm presented in Table I reflects its split functionality design. The overall computational effort is a sum of values proportional to the individual filter lengths, in terms of multiplications, respectively additions. Considering the fact that decompositions can be performed such that $L_i \ll L$, the proposed reduction in complexity represents a migration from a setup difficult to implement on hardware platforms to an attractive solution for multiple adaptive systems configurations.

Table I. Exponential weighted RLS-DCD-T algorithm (filter i).

Initialization :

$\widehat{\mathbf{h}}_i(0) = \mathbf{r}_i(0) = \mathbf{0}_{L_i \times 1},\ \mathbf{R}_i(0) = \xi_i \mathbf{I}_{L_i},\ \xi_i > 0,\ 0 < \lambda_i \leq 1$

For $n = 1, 2, \ldots,$ number of iterations :

$\mathbf{R}_i^{(1)}(n) = \lambda_i \mathbf{R}_i^{(1)}(n-1) + \mathbf{x}_{\widehat{\mathbf{h}}_i}(n)\mathbf{x}_{\widehat{\mathbf{h}}_i}^{(1)}(n)$

$\mathbf{R}_i^{(1)}(n)$ denotes the 1^{st} column of $\mathbf{R}_i^{-1}(n)$

$\mathbf{x}_{\widehat{\mathbf{h}}_i}^{(1)}(n)$ denotes the 1^{st} element of $\mathbf{x}_{\widehat{\mathbf{h}}_i}(n)$

$e_{\widehat{\mathbf{h}}_i}(n) = d(n) - \widehat{\mathbf{h}}_i^T(n-1)\mathbf{x}_{\widehat{\mathbf{h}}_i}(n)$

$\mathbf{p}_{0,i}(n) = \lambda_i \mathbf{r}_i(n-1) + e_{\widehat{\mathbf{h}}_i}(n)\mathbf{x}_{\widehat{\mathbf{h}}_i}(n)$

$\mathbf{R}_i(n)\Delta\mathbf{h}_i(n) = \mathbf{p}_{0,i}(n) \xrightarrow{\text{DCD}} \Delta\widehat{\mathbf{h}}_i(n), \mathbf{r}_i(n)$

$\widehat{\mathbf{h}}_i(n) = \widehat{\mathbf{h}}_i(n-1) + \Delta\widehat{\mathbf{h}}_i(n)$

Using the conventional RLS family of algorithms [2] (i.e., the direct estimation of the global impulse response) could be very costly for large values of L, since the computational complexity order would be $\mathcal{O}(L^2)$. On the other hand, the computational complexity of the RLS-T algorithms is proportional to $\sum_{i=1}^{N} \mathcal{O}(L_i^2)$, which could be much more advantageous when $L_i \ll L$. In addition, since the RLS-T operates with shorter filters, improved performance is expected, as compared to the conventional RLS algorithm. The RLS-DCD-T brings an extra layer of efficiency by performing the same tasks with workloads of order $\sum_{i=1}^{N} \mathcal{O}(L_i)$. These observations are also supported by our preliminary experimental results, which will be reported in future works.

IV. Conclusion

This idea paper has introduced a low-complexity RLS-based adaptive algorithm for the identification of unknown systems based on tensorial decompositions. The resulting RLS-DCD-T algorithm benefits from the low computational requirements of the DCD iterations and could provide performance comparable with other established versions of tensorial based RLS methods. The reduction in complexity for the adaptive filter update process is important. Most importantly, the usage of the DCD iterations allows for the coefficient updates to be performed using only bit-shifts and additions.

Acknowledgement

This work was supported by two grants of the Romanian Ministry of Education and Research, CNCS–UEFISCDI, project no. PN-III-P1-1.1-PD-2019-0340 and project no. PN-III-P1-1.1-TE-2019-0529, within PNCDI III.

References

[1] L.-M. Dogariu et al., "Tensor-based adaptive filtering algorithms," *Symmetry*, vol. 13, id 481 (27 pages), Mar. 2021.

[2] S. Haykin, *Adaptive Filter Theory*. Fourth Edition, Upper Saddle River, NJ, USA: Prentice-Hall, 2002.

[3] Y. V. Zakharov, G. P. White, and J. Liu, "Low-complexity RLS algorithms using dichotomous coordinate descent iterations," *IEEE Trans. Signal Processing*, vol. 56, pp. 3150–3161, Jul. 2008.

 ISBN: 978-1-61208-917-1

Protocols for Underwater Wireless Sensor Networks - Challenges and Solutions

Anne-Lena Kampen
Western Norway University of Applied Sciences
Bergen, Norway
e-mail: alk@hvl.no

Abstract—**The underwater environment poses challenges for communication that can make terrestrial solutions ineffective. However, the mature terrestrial solutions are based on decades of real-world research and experience, proving their sustainability and reliability. Although not suitable for direct replication, it may be wise to take advantage of these proven solutions. With this in mind, it is valuable to study successful terrestrial approaches and evaluate their ability to support the harsh underwater environment, and to assess how procedures and algorithms can be adapted for efficient underwater communication. In this paper, we revisit frequently used Medium Access Control (MAC) protocols and discuss the challenges they face in the underwater environment. In addition, underwater challenges related to multi-hop data collection are discussed. To improve reception reliability in the highly dynamic underwater environment, we focus on broadcast solutions that are constrained to avoid network flooding. Location-based techniques look very promising in this regard. Related to the MAC layer, our recommendation is that underwater communication solutions should focus on preventing collisions at receiver, while reducing the time between packet reception.**

Keywords-UWSN; underwater wireless sensor networks; Medium Access Control MAC; underwater routing.

I. INTRODUCTION

The United Nation (UN) sustainability goal #14, life below water [1], calls for underwater surveillance solutions to monitor the marine environment and strengthen ecosystem knowledge. To this end, sensor networks can be essential building-blocks in systems used by the ocean industries and public surveys for monitoring the seabed and water-column conditions. The network can contribute to sustainable exploitation of underwater resources by monitoring environmental parameters, and ensure responsible growth with well-controlled environmental impact.

Like terrestrial sensor networks, Medium Access Control (MAC) and network layer protocols are important to build sustainable networks. The goal of the MAC is to wisely share the network media between the nodes to provide efficient data collection. The network layer enables data from remote nodes to reach its destination. The protocols must adapt to the technology challenges related to the underwater media, such as low propagation speed, low and dynamic channel capacity, interference, ambient noise and asymmetric links, and so forth. In addition, the sensors are mainly battery charged and battery replacement is unfeasible. Furthermore, the ocean current may move the sensors. Thus, the protocols should provide solutions that cope with the dynamic environments and, simultaneously, reduce the energy consumption of the nodes.

Current underwater wireless solutions are mainly based on underwater acoustic transmission [2]. The signal propagation for acoustic underwater communication is five orders of magnitude slower than light speed; in addition, it is affected by temperature, salinity and depth [3][4]. The low propagation speed presents a fundamental challenge in coordinating the access to the shared communication medium. The room available for medium access control is compressed, and limited channel capacity should not be used for resource reservation processes requiring large protocol overhead.

Network layer protocols establish routing paths to enable multihop transmission, which can be used to increase the area covered by the network and/ or to reduce the output power, i.e., reduce transmission range, and save energy. The routing paths are formed based on specified criteria that aim to support the overall goal for the communication and/or to support overall network goals. For instance, the data can be transmitted over several paths simultaneously to support reliable communication or the data can be sent alternately over different available paths to balance the energy consumption in the network to prevent early depletion of nodes. However, due to the dynamic characteristic of the channel, and potential movement of sensor nodes, it is difficult to construct proactive routing paths, while reactive paths introduce high transmission delay. On the contrary, broadcasting can limit the delay and reduce the need for proactive configuration. In addition, the reliability is improved because the data are transmitted over several paths. However, the broadcast should be constrained to reduce network traffic and limit the energy consumption of the nodes. Thus, the peculiar characteristic of the environment means that protocols used in terrestrial communication require adjustments to provide efficient underwater communication. To this end, the contribution of this paper is to discuss characteristics that are challenging when converting basic terrestrial MAC layer protocols for use in underwater environment. In addition, network layer protocols that enable constrained multicast are investigated. Basic multicast should be avoided to prevent excessive network traffic as well and excessive energy consumption.

The rest of the paper is structured as follows. In Section 2 we present the related work. MAC layer protocols their issues related to the underwater environment are discussed in Section 3. Network layer protocols, and their issues, are

 ISBN: 978-1-61208-917-1

discussed in Section 4. In Section 5 we present the conclusion.

II. RELATED WORK

The increasing interest in life and resources below water has mobilized a wide range of research on underwater sensor networks. The communication protocols are important to enable efficient operation. Thus, a range of solutions are suggested in the literature, and various surveys present and discuss selected solutions focusing on various aspects. A thorough discussion of MAC protocols for underwater acoustic networks is found in [5]. It is emphasized that further studies should focus on methods that handle the long propagation delay in ways that improve the utilization of the available bandwidth. For instance, one way is by allowing concurrent transmission as long as packet-collision at the receiver is prevented. Boukerche and Sun [6] discuss the underwater channel modeling, MAC and routing protocols, and localization schemes. It is pointed out that underwater environment represents a much more complex environment than the hypothesis that the existing approaches are commonly based upon. The complex environment characteristics are the reason that we, for network layer solutions, focus on constrained broadcast rather than single path solutions that are more vulnerable for changing channel characteristics.

Khisa and Moh [7] focus on energy-efficient routing protocols, and categorize the protocols using a new taxonomy. Energy consumption is also very much in focus when discussing localization-based and localization-free routing protocols, along with routing issues in [8]. In the conclusion, Khalid et al. point out that all protocols have pros and cons such that a protocol that is best for all cases cannot be found. The same is pointed out in [9] where routing protocols for acoustic sensor networks are assessed according to feasible application scenarios. An earlier survey that gives a nice overview of routing protocols and network issues is presented in [10]. Terrestrial routing protocols are also compared with Underwater Wireless Sensor Networks (UWSNs) in the survey. The survey presented in [11] focuses on cross-layer designed routing protocols. The authors define cross layer design as a design where algorithms from different layers can exchange information with each other, and point out that layered designs are better for creating adaptive solutions. A substantial part of the protocols suggested for UWSNs do, at least to some degree, follow the definition of cross-layer solutions defined in the paper. For instance, using this definition, all network layer protocols that use location or energy level as selection criteria will be categorized as cross-layer protocols.

Our focus is to present the issues that affect the MAC and network layer protocols. We review basic MAC layer algorithms and describe their weakness related to underwater communication. At the network layer, the focus is on methods that reduce broadcast. Due to the dynamic environment, the links are very unreliable. Broadcast communication is therefore advantageous compared to communication over pre-decided dedicated links. However, simple broadcast is a waste of energy.

III. MAC PROTOCOLS

MAC protocols have a large impact on the overall network performance because they coordinate the nodes' access to the medium. The access must be shared fairly between the nodes, the scarce bandwidth resource must be efficient utilized, packet collisions should be avoided, and the access delay must be limited. In addition, sustainable solutions require energy-efficient operations that lengthen the network lifetime and reduce the management cost. To this end, the impact for the various states of the communication processes must be investigated to develop the most optimal solution. In addition, dynamic environments and low channel capacity require adaptive and bandwidth-efficient protocols.

The access methods generally used can be categorized as fixed-assignment protocols, demand-assigned protocols and random-access protocols [12]. In fixed-assignment protocols, the channel is divided between the nodes such that nodes can access the medium without any risk of collisions. Typical protocols used are Time Division Mutiple Access (TDMA), Frequency Division Multiple Access (FDMA) and Code Division Multiple Access (CDMA). These protocols provide predictable access delay, and efficient utilization of available bandwidth. In addition, no energy is wasted on collisions. However, static resource reservation increases the packet loss probability in the highly dynamic underwater environment. In addition, the assigned resources require signaling to renegotiate resources when the network topology changes or if nodes require more resources due to increased traffic load.

Demand-assigned protocols provide short term channel assignments. Polling schemes belong to this class of protocols. The nodes may emit request for channel allocation and successful allocation is confirmed back to the nodes with description of the allocated resources. The resource may be in terms of number and positions of TDMA slots. Time slotted communication is illustrated in Figure 1. The administration of resources can be distributed to some key-nodes in the network, for instance to cluster heads in

clustered networks. However, network-wide resource reservation is complex as traffic from nodes in adjacent areas can interfere. In addition, underwater currents or seafloor changes may move the nodes. Furthermore, efficient TDMA requires precise synchronization which is challenging in underwater environments due to the long and variable transmission delay, however short periods of static and predictable propagation delay may provide synchronization that is accurate enough [13].

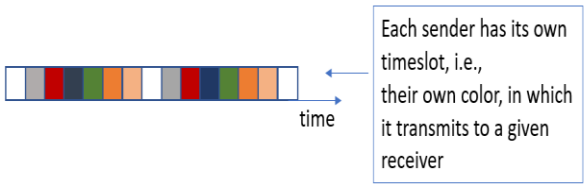

Figure 1. Time slotted communication. TDMA

 ISBN: 978-1-61208-917-1

The nodes in random-access protocols are uncoordinated and operate in a fully distributed manner. ALOHA is one of the earliest and most important protocols in this category. In the simplest version of ALOHA, the nodes transmit the packets as soon as they are generated. Successfully receiving the packet, the receiver transmits an Acknowledgement packet (ACK) back to the sender. If the sender does not receive ACK, it assumes that a collision has occurred. It waits a random amount of time (backoff) before retransmitting the packet. ALOHA works well when the traffic load is low. Under heavier load the number of collisions increases, increasing the delay and energy consumption, and reducing the throughput efficiency. In slotted ALOHA, the time is divided into timeslots, and packet transmission can only start at the beginning of a timeslot. The slot time is long enough to accommodate the longest allowed packets. Thus, only simultaneously transmitted packets can collide. However, because of the long transmission delay, this is not true in underwater communication. In addition, to avoid collisions, the slot length must also take the transmission time as well as packet length into consideration. That is, the transmission time between the sender and the node that is furthest away, but still within the sender's transmission range (interference range), must be considered.

Another popular random-access protocol is Carrier Sense Multiple Access with Collision Avoidance (CSMA/ CA), which is a random-access scheme with carrier sense and collision avoidance through random backoff. Different backoff algorithms can be used, but they roughly follow the following procedure: To avoid disrupting ongoing transmissions the nodes listen (carrier sense) to the channel, and choose a random number of backoff slots within a contention window. After the channel has been idle for a period equal to Distributed Interface Space (DIFS), the backoff value is decremented for each idle timeslot observed on the channel. As soon as the counter expires, the node accesses the medium. See illustration in Figure 2, where node A transmits a packet after the channel has been idle for DIFS plus the time it takes for the backoff value to be counted down. Node B has to wait until the channel has been idle for DIFS before it starts counting down the backoff value. A collision triggers retransmission with a new random selection of backoff time, and for each collision the contention window doubles. This is called exponential backoff. An explicit ACK is sent by the receiver upon successful reception of the packet. Using slotted CSMA, the backoff equals a random number of timeslots. Asymmetric links affect the communication efficiency especially when reliable communication is required. The reason is that when ACK messages are lost, the packets will be re-transmitted. Re-transmitted packets increase network traffic, which increases collision probability and also the energy consumption.

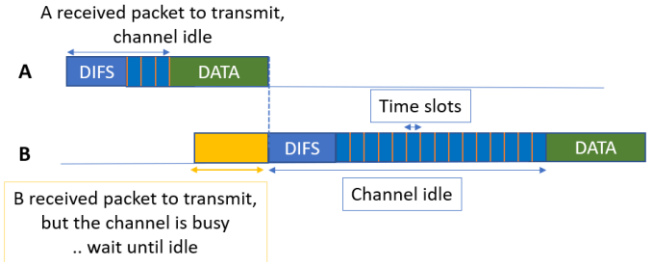

Figure 2. Carrier Sense Multiple Access CSMA

Furthermore, carrier sense protocols are susceptible to hidden node problem and unfair access. The slow propagation speed can lead to unfair access since there is special bias in estimating clear channel. Nodes close to the signal source get a clear channel earlier providing them with more access opportunities [14]. Another spatial unfairness is when nodes closer to the receiver may always win Request To Send (RTS) contentions since their requests are always received earliest [15]. The hidden node problem is due to the distance between the transmitting and receiving node. A transmitting node, N_{T1}, cannot detect activity at the receiver, Ns, that is caused by a sending node, N_{T2}, whose transmission reaches the receiver, but not the node N_{T1}. To reduce the hidden-node problem, Request To Send/ Clear To Send (RTS/CTS) can be used. After the sending node has obtained channel access it sends a RTS packet to the receiver. The packet includes a time-field that indicate the duration of the overall transaction. Successfully receiving the RTS means that there are no hidden nodes that are currently creating interference at the receiver side. The sender replies with an CTS, which also includes the duration time-field. Receiving the CTS the transmitter starts transmitting of the data packet. Thus, signaling the data transmission with both RTS and CTS, reduced the hidden node problem. In addition, neighbors of both the sender and the receiver are informed about the transmission and its duration. To account for the long transmission delay in underwater environment, the nodes must delay data transmission according to the longest possible delay, and the relatively long time-span increases the probability of transmission from a neighboring node. Thus, basic access control processes, such as carrier sense, reservation of the media, and ACK are more time-consuming and more management is required if these processes are to be optimized for neighbors at different distances.

Channel utilization and the first-in-first-out fairness police may also suffer from the long delay. The latter is the case if transmissions arrive out-of-order because the propagation delay from various senders is unequal. Channel utilization is reduced because collision-free reception is not guaranteed although the transmissions from different nodes are collision-free. Likewise, concurrent transmission may not lead to collision [16]. To improve the media utilization, receiver-centric solutions can be used to handle the unequal delay that exists between the various transmitting nodes. Receivers can arrange the transmission time for the transmitters so that collisions are avoided, while avoiding that the time between each received packet is unnecessarily long, such as suggested in [17]. The major challenge of the solution is prediction and management of delays, which

 ISBN: 978-1-61208-917-1

require frequent information exchange between nodes, especially under dynamic channel conditions.

No solution can take all challenges into account. Thus, no solutions fit all scenarios as confirmed in the at-sea-experiment presented in [18], where the performance of three well-known MAC layer protocols, namely CSMA, T-Lohi [19][20], and Distance Aware Collision Avoidance Protocol (DACAP), is evaluated in an extensive sea-test during NATO at-sea campaigns. CSMA is the simplest of these protocols, where, to prevent collisions, the nodes listen to detect if the media is idle before transmission. If not idle, the nodes back-off according to an exponential back-off mechanism after which it again listens for a silent channel. ACK can be used for reliable communication. Applying T-Lohi, the node transmits a reservation-tone, after which it listens to the channel for the duration of a Contention Round (CR). If no other tones are heard during CR, the data packet is transmitted. Otherwise, it enters back-off state for a random number of CR before repeating the procedure. The most advanced of the three protocols is DACAP in which RTS/ CTS is used to reserve the channel. To warn about possible interference, the destination node sends a short warning packet to its sender if it overhears control packets from other nodes after sending its CTS and before receiving the associated data packet. If the sender overhears a control packet, or receives a warning form its destination while waiting for CTS, it aborts data communication. Using two different modems, the results reported in [18] for the three different MAC protocols show similar trends, although the overall protocol performance is significantly affected by the delays and overheads associated with the acoustic modem used. Furthermore, the results presented show that different traffic load, channel conditions and evaluation metric call for different solutions. Basically, solutions should be able to adapt, in a distributed way, to dynamically changing conditions. Using DACAP, the network performance is deteriorated when the traffic load is increased. ACK packet improves packet delivery ratio as long as the link is symmetric, however this is not always the case. CSMA reduces the transmission attempts since the channel is reserved by the data packet itself, however, the whole packet has to be retransmitted when collisions occur. The end-to-end delay of CSMA and DACAP use exponential backoff making the delay increase rapidly with increased number of retransmissions. Not using exponential backoff, T-Lohi has lower end- to- to lay, the price payed is higher packet loss.

In contrast to single-channel protocols discussed so far, multiple-channel protocols rely on several channels for communication to increase network throughput, reduce channel access delay, and potentially save energy. Neighboring nodes can communicate simultaneously, provided that they communicate using unequal data channels. Furthermore, control signals sent on a different channel will not affect the data that is sent. In [21], the control channel is slotted such that each node in a neighborhood is assigned a unique slot. Thus, also control packet are prevented from collisions. The solution suggested in [22] present a quorum-based data channel allocation to prevents collisions. However, generation and management of multichannel protocols is complex, and require advanced modems. In addition, if the nodes are equipped with only one transceiver, it means that they can only work one channel at a time, either on the control channel or on the data channel. When this is the case, the handshaking protocols such as RTS/CTS must be tuned to prevent triple-hidden terminal problem [23]. The triple-hidden problem occurs if two of the nodes in a neighborhood are communicating on a data channel. Simultaneously, another two nodes use the control channel for handshaking and agree to use channel A for data communication. The first two nodes will then be unaware of the data channel that the last two nodes selected. Thus, if the first two nodes want to initiate a new communication, they may select data-channel A, creating a collision.

Central one-hop network solutions simplify media access management and general network complexity at the cost of network coverage and network dynamic. Collisions can easily be avoided using a polling approach where the nodes are prohibited from transmission unless polled by the central node. The polling sequence is not required to be sequential; it can contain repetitions to support nodes with various amount of sensor-data [24]. To approach the throughput gained using TDMA, [25] suggest a centralized approach. The gateway measures the delay to each individual node to organize the nodes' transmission time and sequence. The gateway manages the network operation such that the data from all the nodes are received in strict order, resembling a subdivision frame. Although interesting approaches, they require the nodes to stay awake to listen for polling requests.

To summarize, there is no single solution that works best in all scenarios, and there is probably a need for solutions that can be adapted to dynamic changes. Furthermore, most of the underwater MAC protocols suggested follow terrestrial approach, trying to avoid transmission collision, although this will not guarantee against collision at reception [5]. To efficiently utilize the scarce bandwidth available underwater, the focus should be on the receiver side, solutions must reduce the time between packet reception while simultaneously preventing collisions at the receiver.

IV. NETWORK LAYER PROTOCOLS

Multi-hop communication can be used to increase the area covered by the network, or it can be used to reduce the distance between nodes. The advantage of reducing the distance is that the nodes' output power can be reduced to save energy. Also, the reduced distance can be used to increase the bit rate by increasing the transmission frequency and bandwidth. Furthermore, short distance between nodes increases the granularity of the surveyed area which may be valuable to pick up local variations and trends related to the parameters surveyed. On the other hand, longer distances between nodes in multi-hop networks can reduce equipment and management costs.

Multihop communication entails challenges such as increased network traffic and imbalance in the energy consumption in the network. Traffic increases because data packets must be forwarded, and management information must be exchanged to generate and maintain the routing paths. Energy imbalance occurs since the nodes in the

 ISBN: 978-1-61208-917-1

vicinity of the sink must forward packets for all remote located nodes. Furthermore, the harsh underwater environment makes the generation of routing path more challenging. For instance, it is likely that the quality of a substantial amount of the links are time varying, thus proactively generated paths may not be reliable. Reactively created paths, on the other hand, introduce long delay. In addition, the links may be unidirectional or asymmetric, which makes it difficult to utilize paths that may be well-working and stable for communication in the correct direction. Broadcasting alleviates the challenges related to generating routing paths since all candidate paths are tried, and no specific routing paths needs to be generated. However, the broadcast must be constrained to prevent excessive network traffic, and to reduce the energy consumption of the nodes.

Opportunistic routing [26] can be an efficient method to constrain broadcasting. The basic idea is that all receivers contend to forward packets, i.e., the senders broadcast the packets which are forwarded by the most optimal receiver. Location-based protocols can be used for opportunistic routing in underwater environments. Using a greedy scheme, packets are always forwarded by the node located closest to the sink. This is illustrated in Figure 3, where the green node transmits a packet. The circle around the green node illustrates green node's transmission range. The red node is the destination, i.e., the sink. The orange node is the node inside the green node's transmission range that is closest to the sink. Thus, the orange node forwards the packet. Only local information is used to decide whether the received data should be forwarded, no routing data needs to be exchanged. For instance, each data packet contains information about the destination's location. Nodes that receive the packet start a timer that is proportional to their own distance to the destination. If the node overhears the packet being forwarded by a neighboring node before its own timer reaches zero, it refrains from forwarding the packet. Otherwise, it forwards the packet. The long delay in underwater communication requires that the timer that sets the holding-time (the time between a packet is received until it is potentially forwarded) is wisely set. Two aspects must be considered. First, the timer must be long enough to ensure that a packet forwarded by a more preferred node is received by the less preferred node before the timer of the less preferred node expires. Remember, due to the underwater environment, it takes time for the forwarded packet to reach the less preferred nodes. Second, it is likely that the node in the more preferred location receives the packet later because it is probably located closer to the sink, and further form the transmitter. To sum up: wait until the most-preferred node receives the packet, then wait for the packet relayed by this most-preferred node to reach the less-preferred nodes. Taking both of these aspects into consideration increases the delay in the network. In addition, when the number of potential successor nodes is high, a wide range of distinct holding-time-values is required to prevent multiple node timers from expiring simultaneously. To provide a broad range of distinct holding-time-values, the average delay in the network increases.

Location-based opportunistic protocols require that nodes know their location. GPS is unfeasible as an underwater location service. One method of solving the underwater location problem is to let some dedicated nodes, with known locations, send out beacons at regular intervals. Based on received signal, other nodes can use methods like triangulation to determine their own location. Received power and/ or time delay of acoustic signals offer better precision than when using terrestrial radio signals. However, some nodes may be located such that they cannot receive the beacons emitted to estimate locations. To prevent data from these nodes from being lost, a method such as suggested in [27] can be used: The nodes that do not receive location information use a reactive protocol to send data to the best-located neighbor node.

Routing pipe can be used to reduce the number of potential forwarding nodes, and reduce the probability of excessive network traffic for opportunistic protocols. In addition, it alleviates the increased delay needed to accommodate the broad range of distinct holding-time-values discussed above. Assuming a vector from the sender to the target node, the routing pipe is a cylinder with adjustable radius centered around that vector. Nodes inside the cylinder are candidate forwarding nodes. The transmitted packet carries the position of the sender node, the target node, and the forwarding nodes to enable the receivers to determine whether they are located inside the routing pipe, and whether they are located closer to the destination than the transmitting node. This is illustrated in Figure 4. The green node transmits a packet toward the sink (the red node). All nodes within the green circle encircling the green node are covered by transmission. The packet is forwarded by the

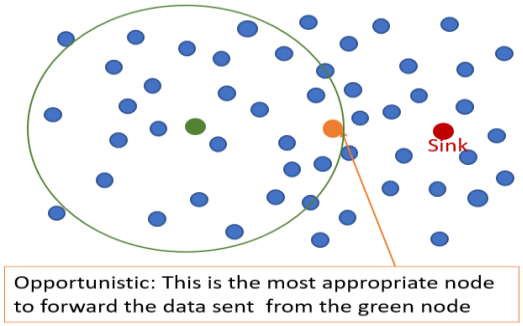

Figure 3. Opportunistic routing.

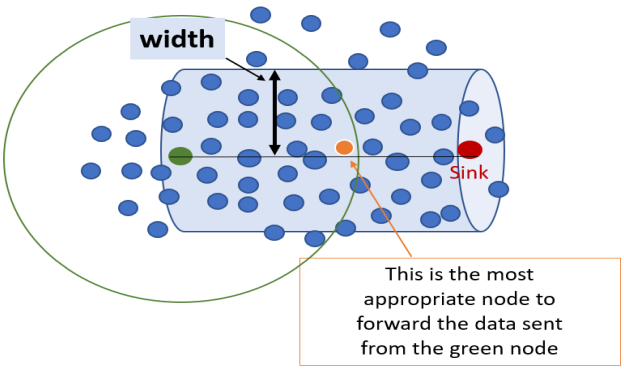

Figure 4. Time slotted communication. TDMA

orange node since it is the node inside the pipe (blue shaded cylinder) that is closest to the sink. Adjusting the width of the cylinder or the transmission range, adjusts the number of candidate forwarders. In [28], to reduce the chances of forwarding data packets, nodes with less energy than the transmitting node intentionally calculates a reduced pipe diameter. Thus, they reduce that chance of being inside the cylinder formed by the sender-receiver vector and diameter. This is done to improve the energy balance in the network.

A challenge related to location-based routing is the void region that may exist in the network. To prevent data loss, some measures are needed to find detours around the potential voids. A simple algorithm for finding detours around voids is to switch to broadcasting when approaching voids regions. Other measures to avoid void generally require that information is exchanged between the nodes. In the depth-based approach suggested in [29], the node examines its neighbors to check whether they can provide positive progress toward the destination. If not, the node requests information from two-hop nodes to adjust its depth such that positive forwarding can be resumed. To reduce the void problem, and improve the Packet Delivery Ratio (PDR), a holding-time that takes several factors into considerations is suggested in [30]. Firstly, a reliability index is calculated based on the energy of the current node and the energy of the forwarding region. In order to limit formation of energy holes and thereby increase the reliability, the forwarding region with the highest energy is selected. Secondly, an advancement factor is used: The depth of the note is calculated so that a small decrease in the depth gives an exponential increase in priority. This reduces the probability of duplicate packet transmissions because the priority difference is significant, even for a low change in depth. Third, a shortest path index is used. It combines the number of hops toward the destination and the average depth of the nodes in the next hop.

Other well-known algorithms used in terrestrial Wireless Sensor Networks (WSNs) to reduce broadcasting, such as probabilistic and counter-based schemes may be well-worth testing in underwater environments. Counter-based schemes are based on the fact that broadcasting a message that has already been broadcasted by several neighboring nodes will not give a substantially increase the area covered. Thus, the nodes are prevented from rebroadcast messages if the expected additional coverage is limited. Basically, the nodes count the number of times a message is received while waiting for medium access. If the counter becomes higher than a threshold, the transmission is canceled, otherwise the message is transmitted [31][32].

In probabilistic schemes, the nodes will rebroadcast messages with a probability P. If P = 1 the data packets are broadcasted. There is a certain probability that no neighbors choose to forward a packet. To ensure the progress of a packet towards the destination, the sender can re-emit the packet if no forwarded packets are heard. However, to ensure the packet's progress, the sender may need to re-emit the packet several times, which increases network traffic. In addition, the packet may have been forwarded by nodes connected over a unidirectional link, which means that the re-emitted packets are a waste of both energy and bandwidth.

To summarize, due to the dynamically changing channel condition and the long propagation delay in the underwater environment, broadcasting may be a better solution than reusing terrestrial routing protocols that generate specific routing paths. Broadcast-based forwarding is likely to improve the probability of packets reaching their intended destination. However, the broadcasting procedure should be constrained to reduce both energy consumption and network traffic.

V. CONCLUSION

MAC and network layer solutions for underwater communication require that characteristics such as long propagation delay, dynamic channel characteristic and limited bandwidth are considered. Long delays are especially challenging for MAC protocols. The time available for access control is reduced, and the limited channel resources should not be depleted by large amount of management traffic. For efficient utilization of the limited channel capacity, the focus should be on the solutions that both reduce the time between received packets, and, at the same time, prevent packet collisions at the receiver.

Dynamic channel properties make it challenging to generate fixed routes. To reduce the probability of packets being lost during forwarding, we recommend to use constrained broadcasting techniques. Location-based techniques seem to be especially promising, and should be further investigated.

In our future work, we will perform extended simulations of some of the protocols we have discussed in this paper. The protocols that show promising simulation results will be further evaluated in experimental tests.

REFERENCES

[1] D. o. E. a. S. A. United Nations, Sustainable Development. "Goal 14." United Nations. https://sdgs.un.org/goals/goal14 (retrieved: October 2021.)

[2] C. M. Gussen et al., "A survey of underwater wireless communication technologies," J. Commun. Inf. Sys, vol. 31, no. 1, pp. 242-255, 2016.

[3] S. Gauni et al., "Design and Analysis of Co-operative Acoustic and Optical Hybrid Communication for Underwater Communication," Wireless Personal Communications, vol. 117, no. 2, pp. 561-575, 2021.

[4] E. Zanaj, E. Gambi, B. Zanaj, D. Disha, and N. Kola, "Underwater wireless sensor networks: Estimation of acoustic channel in shallow water," Applied Sciences, vol. 10, no. 18, p. 6393, 2020.

[5] S. Jiang, "State-of-the-art medium access control (MAC) protocols for underwater acoustic networks: A survey based on a MAC reference model," IEEE communications surveys & tutorials, vol. 20, no. 1, pp. 96-131, 2017.

[6] A. Boukerche and P. Sun, "Design of Algorithms and Protocols for Underwater Acoustic Wireless Sensor Networks," ACM Computing Surveys (CSUR), vol. 53, no. 6, pp. 1-34, 2020.

[7] S. Khisa and S. Moh, "Survey on Recent Advancements in Energy-Efficient Routing Protocols for Underwater Wireless

 ISBN: 978-1-61208-917-1

Sensor Networks," IEEE Access, vol. 9, pp. 55045-55062, 2021.

[8] M. Khalid et al., "A survey of routing issues and associated protocols in underwater wireless sensor networks," Journal of Sensors, vol. 2017, 2017.

[9] Q. Lu and J. Shengming, "A review of routing protocols of underwater acoustic sensor networks from application perspective," in 2016 IEEE International Conference on Communication Systems (ICCS), IEEE, pp. 1-6, 2016.

[10] M. Ayaz, I. Baig, A. Abdullah, and I. Faye, "A survey on routing techniques in underwater wireless sensor networks," Journal of Network and Computer Applications, vol. 34, no. 6, pp. 1908-1927, 2011.

[11] N. Li, J.-F. Martínez, J. M. Meneses Chaus, and M. Eckert, "A survey on underwater acoustic sensor network routing protocols," Sensors, vol. 16, no. 3, p. 414, 2016.

[12] H. Karl and A. Willig, Protocols and architectures for wireless sensor networks. John Wiley & Sons, 2007.

[13] A. A. Syed and J. S. Heidemann, "Time Synchronization for High Latency Acoustic Networks," in Infocom, vol. 6, pp. 1-12, 2006.

[14] W.-H. Liao and C.-C. Huang, "SF-MAC: A spatially fair MAC protocol for underwater acoustic sensor networks," IEEE sensors journal, vol. 12, no. 6, pp. 1686-1694, 2011.

[15] M. A. Hossain, A. Karmaker, and M. S. Alam, "Resolving spatial unfairness problem with reduced-handshaking in underwater acoustic sensor network," in 2017 International Conference on Wireless Communications, Signal Processing and Networking (WiSPNET), IEEE, pp. 2178-2182, 2017.

[16] K. Kebkal, A. Mashoshin, and N. Morozs, "Solutions for underwater communication and positioning network development," Gyroscopy and navigation, vol. 10, no. 3, pp. 161-179, 2019.

[17] N. Chirdchoo, W.-S. Soh, and K. C. Chua, "RIPT: A receiver-initiated reservation-based protocol for underwater acoustic networks," IEEE Journal on Selected Areas in Communications, vol. 26, no. 9, pp. 1744-1753, 2008.

[18] R. Petroccia, C. Petrioli, and J. Potter, "Performance evaluation of underwater medium access control protocols: At-sea experiments," IEEE Journal of Oceanic Engineering, vol. 43, no. 2, pp. 547-556, 2017.

[19] A. A. Syed, W. Ye, and J. Heidemann, "T-Lohi: A new class of MAC protocols for underwater acoustic sensor networks," in IEEE INFOCOM 2008-The 27th Conference on Computer Communications, IEEE, pp. 231-235, 2008.

[20] A. A. Syed, W. Ye, and J. Heidemann, "Comparison and evaluation of the T-Lohi MAC for underwater acoustic sensor networks," IEEE Journal on Selected Areas in Communications, vol. 26, no. 9, pp. 1731-1743, 2008.

[21] C. Zidi, F. Bouabdallah, R. Boutaba, and A. Mehaoua, "MC-UWMAC: A multi-channel MAC protocol for underwater sensor networks," in 2017 International Conference on Wireless Networks and Mobile Communications (WINCOM), IEEE, pp. 1-6, 2017.

[22] F. Bouabdallah, R. Boutaba, and A. Mehaoua, "Collision avoidance energy efficient multi-channel MAC protocol for underwater acoustic sensor networks," IEEE Transactions on Mobile Computing, vol. 18, no. 10, pp. 2298-2314, 2018.

[23] Z. Zhou, Z. Peng, J.-H. Cui, and Z. Jiang, "Handling triple hidden terminal problems for multichannel MAC in long-delay underwater sensor networks," IEEE Transactions on Mobile Computing, vol. 11, no. 1, pp. 139-154, 2011.

[24] W. Liu et al., "APOLL: Adaptive polling for reconfigurable underwater data collection systems," in 2018 OCEANS-MTS/IEEE Kobe Techno-Oceans (OTO), IEEE, pp. 1-9, 2018.

[25] N. Morozs, P. Mitchell, and Y. V. Zakharov, "TDA-MAC: TDMA without clock synchronization in underwater acoustic networks," IEEE Access, vol. 6, pp. 1091-1108, 2017.

[26] V. G. Menon and P. J. Prathap, "Comparative analysis of opportunistic routing protocols for underwater acoustic sensor networks," in 2016 international conference on emerging technological trends (ICETT), IEEE, pp. 1-5, 2016.

[27] S. Lee and D. Kim, "Underwater hybrid routing protocol for UWSNs," in 2013 Fifth International Conference on Ubiquitous and Future Networks (ICUFN), IEEE, pp. 472-475, 2013.

[28] S. M. Mazinani, H. Yousefi, and M. Mirzaie, "A vector-based routing protocol in underwater wireless sensor networks," Wireless Personal Communications, vol. 100, no. 4, pp. 1569-1583, 2018.

[29] R. W. Coutinho, A. Boukerche, L. F. Vieira, and A. A. Loureiro, "Geographic and opportunistic routing for underwater sensor networks," IEEE Transactions on Computers, vol. 65, no. 2, pp. 548-561, 2015.

[30] M. Ismail et al., "Reliable path selection and opportunistic routing protocol for underwater wireless sensor networks," IEEE Access, vol. 8, pp. 100346-100364, 2020.

[31] R. Otnes, P. A. van Walree, H. Buen, and H. Song, "Underwater acoustic network simulation with lookup tables from physical-layer replay," IEEE Journal of Oceanic Engineering, vol. 40, no. 4, pp. 822-840, 2015.

[32] Y.-C. Tseng, S.-Y. Ni, Y.-S. Chen, and J.-P. Sheu, "The broadcast storm problem in a mobile ad hoc network," Wireless networks, vol. 8, no. 2, pp. 153-167, 2002.

 ISBN: 978-1-61208-917-1